Kekulé Superconductivity Induced by Quantum Geometry in Haldane Phases

Yafis Barlas,[1,*] Fan Zhang,[2] and Enrico Rossi[3]
[1]Department of Physics, University of Nevada, Reno, Nevada 89557, USA
[2]Department of Physics, University of Texas at Dallas, Richardson, Texas 75080, USA
[3]Department of Physics, William and Mary, Williamsburg, Virginia 21387, USA

(Received 23 December 2025; revised 11 August 2026; accepted 2 October 2026; published 3 November 2026)

Chiral two-dimensional electron gases, which capture the electronic properties of graphene and rhombohedral graphene systems, exhibit singular momentum-space vortices and are susceptible to interaction-induced topological Haldane phases. Here, we investigate pairing interactions in the inversion-symmetric Haldane phases of chiral two-dimensional electron gases. We demonstrate that the nontrivial band topology of the Haldane phases enhances intravalley ($\mathbf{Q} = \pm 2\mathbf{K}_D$) pair susceptibility relative to intervalley ($\mathbf{Q} = 0$) pair susceptibility, favoring the emergence of a lattice-scale pair-density wave order. When longitudinal acoustic phonons mediate the pairing interaction, the system supports a chiral Kekulè superconducting order at low densities. At higher densities, the phase diagram depends on the parity of the Chern number J. For even parity, an s-wave Kekulè order appears, while for odd parity we find a $\mathbf{Q} = 0$ valley triplet chiral J and a valley singlet s-wave order at different densities. Our findings are relevant to superconductivity in rhombohedral graphene and Kagome metals.

DOI: 10.1103/k5r2-q11w

While significant progress has been made in understanding unconventional superconductivity [1–11] in spin Chern bands of twisted two-dimensional (2D) crystals, the presence of a moiré superlattice often complicates the identification of the underlying mechanisms [12–29]. For instance, it remains unresolved whether the observed superconductivity originates predominantly from band-projected interactions or from novel pairing instabilities intrinsic to topological bands [30–34]. Alternatively, multilayer rhombohedral graphene (RG) has emerged as a promising platform, displaying superconducting phenomenology [35–43] that appears to be as rich as that of twisted 2D crystals [44–47], but without the complexity of a moirè potential. Notably, in RG, superconductivity can even be hosted by a spin-polarized valley Chern band [35–43,45,48], which underscores the necessity to understand the interplay of band geometry and pairing interactions [49].

In ordinary metals, the pair susceptibility typically diverges at zero center-of-mass momentum ($\mathbf{Q} = 0$), favoring uniform superconductivity over finite-momentum pairing at weak coupling [50–52]. In contrast, this Letter demonstrates that the nontrivial topology of a Chern band qualitatively modifies this picture. Previous works have shown that the quantum geometry can strongly affect the response of superconductors to electromagnetic fields, especially in flat-band systems [53–55]. Our results demonstrate a very different key role of quantum geometry. We show that even for standard effective attractive interactions, such as those mediated by acoustic phonons, the quantum geometry of the Bloch states at the Fermi energy can lead to unconventional superconducting states characterized by a finite center-of-mass momentum and a chiral order parameter.

Our conclusions are based on the analysis of superconducting pairing within a Chern band realized in chiral two-dimensional electron gases (C2DEGs). Specifically, we show that in a spin-polarized half-metal phase of RG, the band-projected intravalley pair susceptibility with pair momentum $\mathbf{Q} = \pm 2\mathbf{K}_D$ is enhanced relative to the intervalley pair susceptibility with $\mathbf{Q} = 0$, and depends on the ratio m/μ, where μ is the Fermi energy and m is an interaction-induced Haldane mass [56]. Since this enhancement occurs at high-symmetry points in the Brillouin zone, it naturally favors a lattice-scale pair density wave (PDW) order, previously identified as a Kekulé superconductor in a different context [57].

This enhancement arises from the coherence factors of the Bloch wave functions in the Haldane phase [58], which can be visualized using the $\hat{z}$ component of the pseudospinor field defined by the Hamiltonian on the Bloch sphere, as illustrated in Fig. 1. In the case of intravalley pairing, as depicted in Fig. 1(a), the $\hat{z}$-component pseudospinors point in the same direction, resulting in constructive interference. In contrast, for intervalley pairing shown in Fig. 1(b), the pseudospinors point in opposite directions, leading to destructive interference and a corresponding suppression of the intervalley pair susceptibility. Overall, the pair susceptibility and superconducting phase diagram depend on the parity of the Chern number J. When

*Contact author: ybarlas@unr.edu

 © 2026 American Physical Society

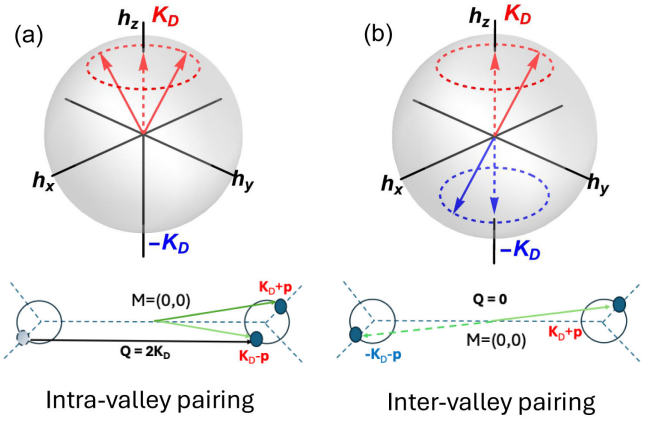


FIG. 1. Hamiltonian pseudospinor field $\hat{\mathbf{h}}$ on the Bloch sphere for (a) intravalley pairing and (b) intervalley pairing in the Haldane phase, with the Fermi surface projection indicated by the dotted red (blue) circles for $\mathbf{K}_D(-\mathbf{K}_D)$ valleys. The projections of $\hat{\mathbf{h}}$ onto the $\hat{z}$ direction for intravalley pairs $\mathbf{p}$ and $-\mathbf{p}$ are parallel, whereas they are antiparallel for intervalley pairs $\mathbf{p}$ and $-\mathbf{p}$. This spinor structure of the Haldane phase results in the suppression of the coherence factors of the intervalley pair susceptibility (see text for details).

longitudinal acoustic phonons mediate the pairing interaction, the system supports a chiral Kekulé superconducting order for low densities n_e. For even values of J the system transitions to an s-wave Kekulé superconducting order when $n_e > n_{e,2}$, with a chiral Kekulé superconducting order appears for $n_e < n_{e,2}$. For odd values of J, a π-phase chiral Kekulé superconducting order appears when $n_e < n_{e,1}$, while in the density regime $n_{e,1} < n_e < n_{e,2}$, we find a $\mathbf{Q} = 0$ valley triplet chiral superconducting state and a valley-singlet s-wave superconductor for $n_e > n_{e,2}$. The chiral superconducting order arises from projected interactions within the topological bands, thereby further reflecting the underlying geometric features of the Haldane phase of C2DEGs.

Model—The continuum model Hamiltonian of a C2DEG with a Chern number J [59] on a projected bipartite lattice is

$$H_0 = \zeta_J p^J \left(\hat{\sigma}_x \cos(J\varphi_{\mathbf{p}}) + \tau_z \hat{\sigma}_y \sin(J\varphi_{\mathbf{p}})\right) + m\hat{\sigma}_z\tau_z, \quad (1)$$

where the Pauli matrices $\hat{\sigma}_i$ act on the pseudospinor $\psi^\dagger_{\tau_z} = (\psi^\dagger_{A,\tau_z}, \psi^\dagger_{B,\tau_z})$, (A, B) are sublattice degrees of freedom to be specified below, $\tau_z = \pm 1$ denote the valleys associated with the Dirac points located at the corners of the hexagonal Brillouin zone (BZ) $\pm\mathbf{K}_D$, $\mathbf{p} = (p_x, p_y)$ is the momentum measured from the Dirac points with $\varphi_{\mathbf{p}} = \tan^{-1}(p_y/p_x)$, and $p = \sqrt{p_x^2 + p_y^2}$. We choose the M point of the BZ as the origin, giving $\pm\mathbf{K}_D = (\pm 2\pi/3, 0)$ and the valley separation $\mathbf{Q} = 2\mathbf{K}_D = (4\pi/3, 0)$. Equation (1) with $m = 0$ describes the minimal model of J-layer RG [60], with the pseudospinor defined on the top $(1, A)$ and bottom (J, B) layers, $\zeta_J = v^J/\gamma_1^{J-1}$, and $v = \sqrt{3}/2\gamma_0 a_0 \sim 673$ meV nm^{-1}, where $\gamma_0 \sim 3.16$ eV and $\gamma_1 \sim 0.445$ eV are the nearest-neighbor intra- and interlayer hopping parameters [42], respectively, and $a = 0.246$ nm is the graphene lattice constant. To highlight the interplay between band geometry and pairing interactions, we neglect trigonal warping for now and address this aspect later.

The Haldane mass term $m\hat{\sigma}_z\tau_z$ results in a quantum anomalous Hall (QAH) state with a Chern number J [56]. This mass term breaks time-reversal symmetry while preserving inversion symmetry. In contrast, a displacement field produces a sublattice staggered potential $\Delta_V\hat{\sigma}_z$ breaking the inversion symmetry. The band dispersion $\epsilon_{\mathbf{p},J,\pm} = \pm(\zeta_J^2 p^{2J} + m^2)^{1/2}$ near the $\pm\mathbf{K}_D$ points is particle-hole and inversion symmetric. The Bloch wave function for the conduction band near $\mathbf{K}_D$ is $|u_{\mathbf{p}}(\mathbf{K}_D)\rangle = (\cos(\theta_{\mathbf{p}}/2)e^{-\imath\tau_z J\varphi_{\mathbf{p}}/2}, \sin(\theta_{\mathbf{p}}/2)e^{\imath\tau_z J\varphi_{\mathbf{p}}/2})$ with $\cos(\theta_{\mathbf{p}}) = m/\epsilon_{\mathbf{p},J,+}$, with inversion symmetry giving $|u_{-\mathbf{p}}(-\mathbf{K}_D)\rangle = \sigma_x|u_{\mathbf{p}}(\mathbf{K}_D)\rangle$. The singularities of the Bloch states near the Dirac points exhibit frustrated momentum-space pseudospin structure, creating a "fertile ground" for spontaneous symmetry breaking [56,61,62].

Interaction-induced Haldane phase in RG—Since our focus is on the superconducting instabilities of the Haldane phase, we consider the simplest case of spinless C2DEGs. In spinless C2DEGs, the corresponding valley-diagonal mass terms are (i) $m\hat{\sigma}_z\tau_z$ and (ii) $\Delta_V\hat{\sigma}_z$. The latter leads to a valley Hall effect, because time-reversal symmetry ensures that the Berry curvatures at the two valleys are equal in magnitude but opposite in sign. In contrast, the former induces a QAH effect with $\sigma_{xy} = Je^2/h$, since inversion symmetry dictates that the Berry curvatures at the two valleys are identical, resulting in a nontrivial Chern number.

A series of experiments [32,33,63,64] has provided compelling evidence for interaction-driven Haldane phase in RG systems ranging from bilayer to pentalayer. In particular, the QAH conductance is quantized at $5e^2/h$ in pentalayer RG at zero magnetic field [32]. Effective in these states, only one spin contributes to the QAH effect [56]. Our mean-field analysis for spinless C2DEGs (see End Matter) reveals that a short-ranged valley-dependent negative interaction $u_\perp < 0$ in the $\boldsymbol{\tau}_\perp \equiv \boldsymbol{\tau} \times \tau_z$ channel leads to a spontaneous QAH state, whereas $u_\perp > 0$ yields a fully layer-polarized state. The interaction-induced Haldane mass term m depends on J, which can be significant: $m \sim 50$ meV for $J = 4, 5$ for an hBN-encapsulated device with a dielectric constant $\epsilon \sim 5$, for gate-screened interactions with gate distance $d = 10$ nm. Since mean-field theory tends to overestimate interaction-induced gaps, we take $m \neq 0$ as a tunable parameter.

Pair susceptibility in the Haldane phase—One key finding of this Letter is that the pair susceptibility of the

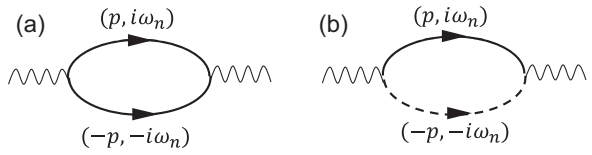


FIG. 2. Feynman diagrams for the (a) intra- and (b) intervalley pair susceptibility of chiral 2DEGs. The solid (dotted) lines denote the band-projected electron propagator of the $\mathbf{K}_D(-\mathbf{K}_D)$ valleys.

Haldane Chern bands is strongly governed by the topologically enforced geometrical properties of the Bloch states, leading to qualitatively distinct superconductivity compared to that of trivial bands. For a generic two-orbital Hamiltonian of the form $H_0 = \hat{\boldsymbol{\sigma}} \cdot \mathbf{h}(\mathbf{k})$, where $\mathbf{h}(\mathbf{k})$ defines the momentum-dependent Hamiltonian field, the projected pair susceptibility $\Pi(\mathbf{q})$ in the σ_0 channel (see Fig. 2) can be expressed as (see Supplemental Material [65])

$$\Pi(\mathbf{q}) = \int \frac{d^2\mathbf{k}}{(2\pi)^2} \frac{g(\mathbf{k}, \mathbf{k}+\mathbf{q})}{\xi_{\mathbf{k}+\mathbf{q}} + \xi_{-\mathbf{k}}} \left(\frac{1 + \hat{\mathbf{h}}_{\mathbf{k}+\mathbf{q}} \cdot \hat{\mathbf{h}}_{-\mathbf{k}}}{2} \right), \quad (2)$$

where $\hat{\mathbf{h}}_{\mathbf{k}} = (\hat{h}_x(\mathbf{k}), \hat{h}_y(\mathbf{k}), \hat{h}_z(\mathbf{k}))$ is the normalized Hamiltonian vector field $\hat{\mathbf{h}}_{\mathbf{k}} = \mathbf{h}_{\mathbf{k}}/|\mathbf{h}_{\mathbf{k}}|$, $\xi_{\mathbf{k}} = \epsilon_{\mathbf{k}} - \mu$ denotes the energy measured from the Fermi surface, and $g(\mathbf{k}, \mathbf{k}+\mathbf{q}) = 1 - n_F(\xi_{\mathbf{k}+\mathbf{q}}) - n_F(\xi_{-\mathbf{k}})$, $n_F(\epsilon) = (e^{\beta\epsilon} + 1)^{-1}$ is the Fermi-Dirac distribution with $\beta = 1/(k_B T)$, and $\mathbf{k} \in \mathrm{BZ}$.

As illustrated in Fig. 1, $\mathbf{q} = 0 + \mathbf{p}$ corresponds to the intervalley pair susceptibility, whereas $\mathbf{q} = 2\mathbf{K}_D + \mathbf{p}$ denotes the intravalley pair susceptibility. Because of the topological nature of the band $\hat{\mathbf{h}}_{\mathbf{K}_D} \sim (0, 0, 1)$ and $\hat{\mathbf{h}}_{-\mathbf{K}_D} \sim (0, 0, -1)$. Therefore, the coherence factors of intervalley pair susceptibility vanish as $(1 + \hat{\mathbf{h}}_{\mathbf{p}} \cdot \hat{\mathbf{h}}_{-\mathbf{p}})/2 \to 0$, while the intravalley pair susceptibility is unaffected, $(1 + \hat{\mathbf{h}}_{\mathbf{p}} \cdot \hat{\mathbf{h}}_{-\mathbf{p}+2\mathbf{K}_D})/2 \to 1$ (see Fig. 1). Thus, intravalley pairing remains robust near the $\pm\mathbf{K}_D$, whereas intervalley pairing is suppressed due to topologically enforced destructive interference of band geometry.

Away from the Dirac points, the intravalley (S) and intervalley (D) pair susceptibilities, denoted by $\Pi_S = \Pi(\mathbf{Q} = 2\mathbf{K}_D)$ and $\Pi_D = \Pi(\mathbf{Q} = 0)$, depend on the ratio of the Haldane gap m to the Fermi energy μ, Chern number parity, and can be expressed as

$$\Pi_a = \frac{N_0}{(1-x^2)^\alpha} \log\left(\frac{E_c}{T}\right) f_a(x) + \cdots, \quad (3)$$

where $\cdots$ denotes nonsingular terms, $a = S(D)$ denotes the intra- and intervalley pairing, $N_0 = x^{1-\eta}/(2\pi J \zeta_J^\eta m^{1-\eta})$, denotes the characteristic density of states, with $\alpha = 1 - 1/J$, $\eta = 2/J$, $E_c \sim \gamma_1$ is the high-energy cutoff, and we have set the Boltzmann constant $k_B = 1$. The intravalley (S) and intervalley (D) pair susceptibilities depend on $x = m/\mu$ through the functions $f_S(x)$ and $f_D(x)$. For even Chern numbers $f_S(x) = 1$ and $f_D(x) = (1 - x^2)/2$, while for odd Chern numbers $f_S(x) = x^2$ and $f_D(x) = (1 - x^2)/2$. Therefore, for even values of J, $\Pi_S > \Pi_D$ throughout the physically relevant range $x \in (0, 1]$. Alternatively, for odd values of J, $\Pi_S > \Pi_D$ requires $x > 1/\sqrt{3}$. In both cases, the geometric suppression of intervalley coherence represents a hallmark of pairing in the Haldane Chern bands.

Longitudinal acoustic phonon-mediated pairing—To determine whether the enhanced intravalley pair susceptibility leads to an intravalley superconducting state, we must specify a model for the pairing interaction. Our estimates indicate that longitudinal acoustic phonons provide the leading contribution to the effective pairing interaction for a circular Fermi surface (see Supplemental Material [65]). Consequently, we neglect the contribution of optical phonons in our analysis. We note, however, that optical phonons correspond to an off-diagonal electron-phonon coupling in orbital space [23,66] and therefore favor intervalley pairing (see End Matter).

Since translational symmetry requires that the interaction is explicitly independent of $\mathbf{Q}$, any $\mathbf{Q}$ dependence of the pairing interaction must arise from the projection onto the Haldane Chern bands. By employing a continuum model for the electron-phonon coupling and performing a Schrieffer-Wolff transformation on the band-projected interaction, we arrive at the generic form of the effective pairing interaction (see End Matter) with two Fermi surfaces at different valleys,

$$\begin{aligned} H_{\mathrm{pair}} = \sum_{\mathbf{p},\mathbf{p}'} \Big[& G_1(\mathbf{p}, \mathbf{p}') a^\dagger_{\mathbf{p}} b^\dagger_{-\mathbf{p}} b_{-\mathbf{p}'} a_{\mathbf{p}'} \\ & + G_2(\mathbf{p}, \mathbf{p}') a^\dagger_{\mathbf{p}} b^\dagger_{-\mathbf{p}} a_{-\mathbf{p}'} b_{\mathbf{p}'} \\ & + G_3(\mathbf{p}, \mathbf{p}') a^\dagger_{\mathbf{p}} a^\dagger_{-\mathbf{p}} b_{-\mathbf{p}'} b_{\mathbf{p}'} \\ & + G_4(\mathbf{p}, \mathbf{p}') a^\dagger_{\mathbf{p}} a^\dagger_{-\mathbf{p}} a_{-\mathbf{p}'} a_{\mathbf{p}'} + (a \leftrightarrow b) \Big], \end{aligned} \quad (4)$$

where the electron creation operators at $\mathbf{K}_D(-\mathbf{K}_D)$ are defined as $c^\dagger_{\mathbf{K}_D+\mathbf{p}} = a^\dagger_{\mathbf{p}}$ and $c^\dagger_{-\mathbf{K}_D+\mathbf{p}} = b^\dagger_{\mathbf{p}}$. Because of inversion symmetry, the interaction matrix elements $G_i(\mathbf{p}, \mathbf{p}')$, satisfy $G_1(\mathbf{p}, \mathbf{p}') = 2G_4(\mathbf{p}, \mathbf{p}')$ and $G_2(\mathbf{p}, \mathbf{p}') = 2G_3(\mathbf{p}, \mathbf{p}')$. Near the Fermi surface $p_x = p_F \cos(\varphi_{\mathbf{p}})$, $p_y = p_F \sin(\varphi_{\mathbf{p}})$ and $|\mathbf{p}| \sim |\mathbf{p}'| \sim p_F$, the interaction matrix elements can be expressed as

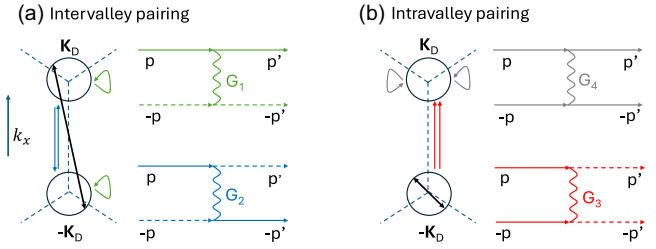


FIG. 3. (a) Feynman diagrams for intervalley scattering interaction G_1 and intervalley exchange interaction G_2, and (b) Feynman diagrams for intravalley scattering interaction G_4 and pair tunneling G_3. The solid (dotted) lines correspond to the electron propagator in the valley $\mathbf{K}_D$ ($-\mathbf{K}_D$). The colors correspond to the microscopic interactions on the circular Fermi surfaces for both intervalley and intravalley pairing.

$$G_4 = -G_0 e^{-\imath J\Phi}\left(\frac{e^{\imath J\varphi_{\mathbf{p}}}(\xi_p+\mu-m)}{2(\xi_p+\mu)}+\frac{e^{\imath J\varphi_{\mathbf{p}'}}(\xi_p+\mu+m)}{2(\xi_p+\mu)}\right)^2,$$
$$G_3 = -\frac{G_0}{2}\left[1+(-1)^J\cos(J\Phi)\right]\left(1-\frac{m^2}{(\xi_p+\mu)^2}\right), \quad (5)$$

where $\Phi = \varphi_{\mathbf{p}} + \varphi_{\mathbf{p}'}$ and the pairing interaction $G_0 = 9.24\times10^{-8}(D/(\hbar v_s))^2 \sim 123\ \mathrm{meV\,nm^2}$, with $D\sim$ 15 eV denoting the deformation field [67], and $v_s \sim 2\times 10^4$ m/s is the phonon sound velocity [24,68]. In Eq. (4), the interactions G_1 and G_2, which denote intervalley scattering and intervalley exchange, as indicated in Fig. 3(a), naturally lead to a conventional superconducting state. Intravalley pairing results from G_4 and G_3, which label intravalley scattering and pair tunneling between the two valleys, as shown in Fig. 3(b).

To determine the leading pairing instability, we decompose each interaction $G_{i,l}$ into the angular momentum channels $l = 0, J, -J$. The renormalization group flow equations (see Supplemental Material [65]) for the pairing interactions $G_{i,l}$ can be expressed as

$$\dot{g}_{1,l} = -[g_{1,l}^2+g_{2,l}^2]f_D(x), \quad \dot{g}_{2,l} = -2f_D(x)g_{1,l}g_{2,l}, \quad (6)$$

$$\dot{g}_{4,l} = -[g_{4,l}^2+g_{3,l}^2]f_S(x), \quad \dot{g}_{3,l} = -2f_S(x)g_{3,l}g_{4,l}, \quad (7)$$

where $g_{i,l}(x) = N_0 G_{i,l}/(1-x^2)^\alpha$ and $\dot{g}_{i,l} = dg_{i,l}/dt$, where $t = \log(\omega_D/T)$ and $\omega_D \sim 0.2$ eV denotes the Debye energy. Equations (6) and (7) can be solved by making the substitution $g_{\pm,l}^{\mathrm{intra}} = g_{4,l} \pm g_{3,l}$, $g_{\pm,l}^{\mathrm{inter}} = g_{1,l} \pm g_{2,l}$ which gives

$$g_{\pm,l}^{\mathrm{intra}} = \frac{g_{\pm,l}^{\mathrm{intra}}}{1+f_S(x)g_{\pm,l}^{\mathrm{intra}}t}, \qquad g_{\pm,l}^{\mathrm{inter}} = \frac{g_{\pm,l}^{\mathrm{inter}}}{1+f_D(x)g_{\pm,l}^{\mathrm{inter}}t}. \quad (8)$$

The superconducting critical temperature for each pairing channel is determined from the poles of Eq. (8), and depends on the parity of the C2DEG, as discussed below.

For even values of J, the coherence factor $f_D(x) = (1-x^2)/2$ in Eq. (6), arising from the quantum geometric properties of the Haldane phase, leads to the suppression of intervalley pairing. The critical temperature for the intravalley (S) pairing [with $f_S(x) = 1$] is $T_c^S(x) = \omega_D \exp(-1/|g_{+,l}^{\mathrm{intra}}|)$, higher than that of the intervalley (D) pairing, $T_c^D(x) = \omega_D \exp\left(-2/[(1-x^2)|g_{+,l}^{\mathrm{inter}}|]\right)$. As shown in Fig. 4(a), the ratio T_c^D/T_c^S is exponentially suppressed, indicating that for even parity the intravalley pairing dominates over the intervalley pairing for all values of x. This exponential dependence is a direct result of the ratio of the even-parity inter- and intravalley pair susceptibilities Π_D/Π_S as derived in Eq. (3).

Since intravalley pairing dominates for even values of J we focus on the interaction matrix elements associated with $G_4(\mathbf{p},\mathbf{p}')$ and $G_3(\mathbf{p},\mathbf{p}')$. For even chirality J, $(g_{+,l} > g_{-,l})$, with $G_{+,0} = -G_0(1-x^2)$, $G_{+,J} = -G_0(1-x)/2$ and $G_{+,-J} = -G_0(1+x)/2$. As $G_{+,-J} > G_{+,0} > G_{+,J}$ for $x_c > 0.5$ we find that the chiral-J Kekulé superconductor has the largest T_c^S when $k_F < (\sqrt{3}m/\zeta_J)^{1/J}$ corresponding to the densities $n_e < n_{e,2}$ with $n_{e,2} = 1/(2\pi)(\sqrt{3}m/\zeta_J)^{2/J}$. The superconducting order parameter is given by $\Delta(\mathbf{r}) = \Delta\cos(2\mathbf{K}_D\cdot\mathbf{r}+\theta)$ (where θ corresponds to the relative phase difference between the valleys). Based on the

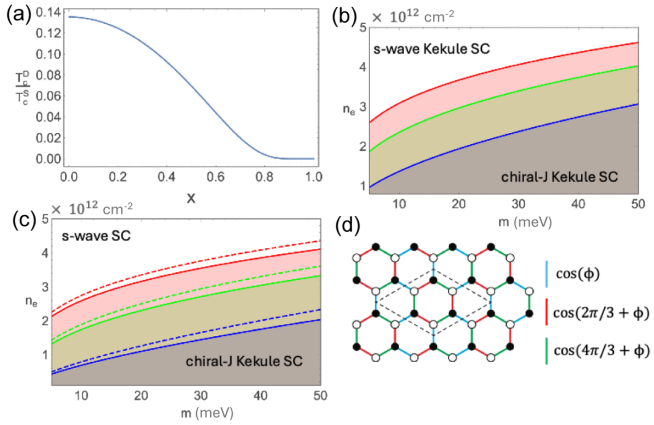


FIG. 4. (a) The ratio of the intervalley critical temperature (T_c^D) to the intravalley critical temperature (T_c^S) as a function of x. (b) Phase diagram for the even chirality C2DEG model of J-layer RG with $J = 4$, 6, and 8 in increasing order. The electron density n_e is in units of cm^{-2} and the Haldane mass is in meV. At low densities, $n_e < n_{e,2}$ the chiral-J Kekulé superconducting channel dominates. (c) Phase diagram for the odd chirality C2DEG model of J-layer RG with $J = 3$, 5, and 7 in increasing order, with the same axis label as in (b). The chiral-J Kekulé superconducting channel dominates for $n_e < n_{e,2}$, giving way to $\mathbf{Q} = 0$ valley triplet chiral superconductivity for $n_{e,1} < n_e < n_{e,2}$, with the phase boundary indicated by the solid line. Conventional valley singlet s-wave superconductivity dominates for $n_e > n_{e,2}$, with the dashed line indicating the phase boundary. (d) Schematic of the Kekulé superconductor on the projected honeycomb lattice, with the superconducting unit cell indicated by the dotted lines.

minimal chiral model, we obtain a phase diagram of superconductivity in Fig. 4(b) for even-parity chiral two-dimensional electron gases (2DEGs) in the (n_e, m) parameter space for different values of $J = 4$, 6, and 8. To ensure a simply connected Fermi surface, we assume that the electron density $n_e \geq 0.8 \times 10^{12}$ cm^{-2}, sufficiently large [42,45] to avoid the three-pocket and annulus Fermi surfaces induced by trigonal warping. As discussed in the End Matter, the superfluid stiffness of the chiral-J Kekulé state scales as $n_e^{J/2}$. There, we also calculate the mean-field critical temperature of the chiral-J Kekulé state in the range $T_c^S \sim 90.8$ mK–13.5 K.

The superconducting phase diagram is quite different for odd-parity chiral 2DEGs, as the intravalley pairing only dominates the intervalley pairing when $x > 1/\sqrt{3}$. Therefore, the chiral Kekulé superconducting order has the highest T_c, when $n_e < n_{e,1}$ with $n_{e,1} = 1/(2\pi)(\sqrt{2}m/\zeta_J)^{2/J}$. Since $G_{-,-J} = -G_0/2(1+x)$ is the dominant channel for odd parity, the intravalley pairing order exhibits an π phase resulting in a Kekulé superconductor with the order parameter $\Delta(\mathbf{r}) = \Delta \sin(2\mathbf{K}_D \cdot \mathbf{r} + \theta)$. $G_{-,J}$ remains the dominant channel for $1/2 < x < 1/\sqrt{3}$, resulting in a valley-triplet π-phase chiral-J intervalley superconducting order for the density regime $n_{e,1} < n_e < n_{e,2}$. However, when $n_e > n_{e,2}$, $G_{+,0} = -G_0(1-x^2)$ becomes the dominant channel, we get a conventional valley singlet s-wave superconductor with $\mathbf{Q} = 0$. Figure 4(c) shows the superconducting phase diagram for the odd-parity chiral 2DEGs as a function of (n_e, m).

Interestingly, for both parities, the presence of a valley degree of freedom permits even-order pairing channels, including a momentum-independent s-wave pairing when $\mu > m$. However, the s-wave pairing channel is suppressed as $\mu \to m$, given $G_{+,0} = -G_0(1-x^2)$. This suppression originates from a combination of the Pauli exclusion principle and the quantum geometric properties of the Haldane phase. At the Dirac points $(\pm\mathbf{K}_D)$, the sublattice and valley degrees of freedom become coincident and act as a single pseudospin, thereby forbidding local (contact) interactions and rendering s-wave Kekulé order incompatible. Consequently, this enhances the relative stability of the chiral-J Kekulé order, which emerges as the dominant channel in this regime. Moreover, due to the presence of a nonzero pair tunneling channel $G_{3,l}$, we expect the chiral-J Kekulé state to be robust to the application of a displacement field, so long as $\Delta_V < m$.

Chiral Kekulé superconductivity—The proposed superconducting state exhibits a spatial Kekulé pattern on the projected bipartite lattice, indicated in Fig. 4(d), and notably, the size of the superconducting unit cell is tripled. The odd chiral-J Kekulé superconductor is a valley triplet with the spontaneously broken symmetry $\mathrm{U}(1) \otimes O_V(3) \otimes \mathbb{Z}_3$, where the U(1) is associated with the overall superconducting phase, $O_V(3)$ is the valley symmetry, and $\mathbb{Z}_3$ is related to the lattice translational symmetry. Alternatively, the even chiral-J Kekulé superconductor must be a valley singlet with the spontaneously broken symmetry $\mathrm{U}(1) \otimes \mathbb{Z}_3$.

Unlike the phase-modulated superconductors revealed in the quarter-metal regime [42,45], the Kekulé superconductors in the half-metal regime are characterized by a spatial modulation of the amplitude of the superconducting order parameter [Fig. 4(d)]. Resolving the Kekulé superconductor would require atomic-scale measurements of the superconducting gap or related Bogoliubov quasiparticle features as a function of position on the lattice, which can be directly probed by scanning tunneling microscopy. At nanometer length scales, it would show a fully gapped spectrum associated with the Bogoliubov quasiparticles of the chiral superconducting state. This provides a clear distinction from a conventional Kekulé lattice distortion, which involves an actual modulation of the lattice [69,70].

Kekulé superconducting textures have previously been proposed for Dirac fermions in graphene, arising from nearest-neighbor pairing interactions [57,71]. However, the mechanism we describe here is fundamentally different: it originates from topologically enforced geometric constraints of the Bloch wave functions, which enhances the pair susceptibility at large momenta $(\pm 2\mathbf{K}_D)$. As such, this Kekulé superconducting order can emerge from a broad class of attractive interactions in the Haldane phase of C2DEGs, independent of the detailed microscopic pairing mechanism.

In RG, trigonal warping of the bands, due to remote hopping processes, induces Lifshitz transitions [72], wherein the Fermi surface evolves from being circularly connected to an annular Fermi surface or a set of disconnected pockets. For tetralayer RG, this transition occurs in the half-metal regime at an electron density of $n_e \sim 0.4 \times 10^{12}$ cm^{-2} near zero displacement field [42,45]. Even above such a density, where the Fermi surface remains connected, it loses its azimuthal symmetry due to trigonal warping. In the presence of a trigonal warping energy scale E_{tri}, the weak-coupling enhancement of the intravalley pair susceptibility is cut off by E_{tri}, and Eq. (3) retains the same functional form, but with $\log(E_c/T) \to \log(E_c/E_{\mathrm{tri}})$. Consequently, for even chirality, a critical pairing strength $G_{+,-J} = -(1-x^2)^{\alpha}/[N_0 \log(E_c/E_{\mathrm{tri}})]$ is required to stabilize Kekulé superconductivity.

Multiple superconducting phases have been detected in bilayer to hexalayer RG [44–47] in the fully layer-polarized states, induced by displacement fields. However, more recently, superconductivity has been observed in doped layer-antiferromagnetic ground states near zero displacement field [46], notably, in the transition region between the fully layer-polarized and layer-antiferromagnetic states, where the Haldane phase is expected to occur. In ultraclean suspended bilayer graphene, an anomalous Hall state with $m \sim 1-3$ meV has been inferred experimentally [73,74], while in hBN-encapsulated pentalayer RG devices a QAH state with $m \sim 10-15$ meV has been reported

[32]. It would be valuable to investigate our proposal for superconducting states that arise at zero or small displacement fields in these regimes.

Assuming the Haldane phase is energetically favored, the remaining competition involves either a charge density wave or an intervalley coherent phase, which leads to a Kekulé lattice distortion [69,70]. Intervalley coherence is typically favored only near charge neutrality ($\mu = 0$) [75]; however, in the presence of a Fermi surface ($\mu \neq 0$) the leading instability is toward superconductivity. Although the Kekulé distortion can be driven by optical phonons [69,70], our estimates in RG indicate that acoustic phonons play a stronger role. Charge-density-wave order is also unlikely, as it generally requires Fermi-surface nesting in the particle-hole channel, which is subleading in our case. Taken together, these considerations suggest chiral Kekulé superconducting state dominates at low densities for a connected Fermi surface in RG.

Discussions and outlook—In conventional metals, the emergence of PDWs typically requires strong correlation effects or fluctuations tied to lattice-scale physics, often leading to modulation periods incommensurate with the crystalline unit cell [76–93]. In contrast, we showed that in the Haldane phase of C2DEGs, the pair susceptibility is enhanced at finite momentum due to the topologically enforced quantum geometry of the Bloch wave functions. This enhancement occurs at high-symmetry points in the Brillouin zone, naturally favoring the formation of lattice-scale PDW states even in the weak-coupling regime. Unlike conventional scenarios that rely on strong-coupling mechanisms, competing orders, or fluctuation-driven instabilities, the quantum geometric mechanism proposed here provides a topologically protected mechanism to realize a lattice-scale PDW order in other chiral Chern bands of 2D crystals and layered materials.

Acknowledgments—Work by Y. B. was supported in part by the DOE EPSCoR program under Award No. DE-SC0022178, and a grant from NIST. F. Z. was supported by the National Science Foundation under Grants No. DMR-2414726, No. DMR-1945351, and No. DMR-2324033 and by the Welch Foundation under Grant No. AT-2264-20250403. Work by E. R. was funded by the US Department of Energy, Office of Basic Energy Sciences, via Award No. DE-SC0022245. Y. B. and E. R. recognize the Kavli Institute for Theoretical Physics (KITP) for hosting as part of the moire24 program, which is supported by NSF No. PHY-2309135, where part of this research was performed.

Data availability—There are no publicly available research data or software supporting this manuscript. Requests for further information or data should be sent to the authors.

[1] Y. Cao, V. Fatemi, S. Fang, K. Watanabe, T. Taniguchi, E. Kaxiras, and P. Jarillo-Herrero, Nature (London) **556**, 43 (2018).
[2] M. Yankowitz, S. Chen, H. Polshyn, Y. Zhang, K. Watanabe, T. Taniguchi, D. Graf, A. F. Young, and C. R. Dean, Science **363**, 1059 (2019).
[3] Y. Cao, V. Fatemi, A. Demir, S. Fang, S. L. Tomarken, J. Y. Luo, J. D. Sanchez-Yamagishi, K. Watanabe, T. Taniguchi, E. Kaxiras, R. C. Ashoori, and P. Jarillo-Herrero, Nature (London) **556**, 80 (2018).
[4] J. M. Park, Y. Cao, K. Watanabe, T. Taniguchi, and P. Jarillo-Herrero, Nature (London) **590**, 249 (2021).
[5] Y. Cao, J. M. Park, K. Watanabe, T. Taniguchi, and P. Jarillo-Herrero, Nature (London) **595**, 526 (2021).
[6] J.-X. Lin, P. Siriviboon, H. D. Scammell, S. Liu, D. Rhodes, K. Watanabe, T. Taniguchi, J. Hone, M. S. Scheurer, and J. I. A. Li, Nat. Phys. **18**, 1221 (2022).
[7] H. D. Scammell, J. I. A. Li, and M. S. Scheurer, 2D Mater. **9**, 025027 (2022).
[8] Y. Xia, Z. Han, K. Watanabe, T. Taniguchi, J. Shan, and K. F. Mak, Nature (London) **637**, 833 (2025).
[9] Y. Guo, J. Pack, J. Swann, L. Holtzman, M. Cothrine, K. Watanabe, T. Taniguchi, D. G. Mandrus, K. Barmak, J. Hone, A. J. Millis, A. Pasupathy, and C. R. Dean, Nature (London) **637**, 839 (2025).
[10] G. W. Burg, E. Khalaf, Y. Wang, K. Watanabe, T. Taniguchi, and E. Tutuc, Nat. Mater. **21**, 884 (2022).
[11] H. Zhou, L. Holleis, Y. Saito, L. Cohen, W. Huynh, C. L. Patterson, F. Yang, T. Taniguchi, K. Watanabe, and A. F. Young, Science **375**, 774 (2022).
[12] T. J. Peltonen, R. Ojajärvi, and T. T. Heikkilä, Phys. Rev. B **98**, 220504(R) (2018).
[13] H. C. Po, L. Zou, A. Vishwanath, and T. Senthil, Phys. Rev. X **8**, 031089 (2018).
[14] C. Xu and L. Balents, Phys. Rev. Lett. **121**, 087001 (2018).
[15] J. F. Dodaro, S. A. Kivelson, Y. Schattner, X. Q. Sun, and C. Wang, Phys. Rev. B **98**, 075154 (2018).
[16] X. Y. Xu, K. T. Law, and P. A. Lee, Phys. Rev. B **98**, 121406(R) (2018).
[17] C.-C. Liu, L.-D. Zhang, W.-Q. Chen, and F. Yang, Phys. Rev. Lett. **121**, 217001 (2018).
[18] H. Isobe, Noah F. Q. Yuan, and L. Fu, Phys. Rev. X **8**, 041041 (2018).
[19] J. González and T. Stauber, Phys. Rev. Lett. **122**, 026801 (2019).
[20] T. Cea, N. R. Walet, and F. Guinea, Phys. Rev. B **100**, 205113 (2019).
[21] Y.-Z. Chou, F. Wu, J. D. Sau, and S. Das Sarma, Phys. Rev. Lett. **127**, 217001 (2021).
[22] V. o. T. Phong, P. A. Pantaleón, T. Cea, and F. Guinea, Phys. Rev. B **104**, L121116 (2021).
[23] F. Wu, A. H. MacDonald, and I. Martin, Phys. Rev. Lett. **121**, 257001 (2018).
[24] F. Wu, E. Hwang, and S. Das Sarma, Phys. Rev. B **99**, 165112 (2019).
[25] B. Lian, Z. Wang, and B. A. Bernevig, Phys. Rev. Lett. **122**, 257002 (2019).
[26] Y. W. Choi and H. J. Choi, Phys. Rev. B **98**, 241412(R) (2018).

[27] R. Ojajärvi, T. Hyart, M. A. Silaev, and T. T. Heikkilä, Phys. Rev. B **98**, 054515 (2018).
[28] T. Cea and F. Guinea, Proc. Natl. Acad. Sci. U.S.A. **118**, e2107874118 (2021).
[29] E. Khalaf, S. Chatterjee, N. Bultinck, M. P. Zaletel, and A. Vishwanath, Sci. Adv. **7**, eabf5299 (2021).
[30] T. Han, Z. Lu, G. Scuri, J. Sung, J. Wang, T. Han, K. Watanabe, T. Taniguchi, H. Park, and L. Ju, Nat. Nanotechnol. **19**, 181 (2024).
[31] Z. Lu, T. Han, Y. Yao, A. P. Reddy, J. Yang, J. Seo, K. Watanabe, T. Taniguchi, L. Fu, and L. Ju, Nature (London) **626**, 759 (2024).
[32] T. Han, Z. Lu, Y. Yao, J. Yang, J. Seo, C. Yoon, K. Watanabe, T. Taniguchi, L. Fu, F. Zhang, and L. Ju, Science **384**, 647 (2024).
[33] Y. Sha, J. Zheng, K. Liu, H. Du, K. Watanabe, T. Taniguchi, J. Jia, Z. Shi, R. Zhong, and G. Chen, Science **384**, 414 (2024).
[34] Z. Lu, T. Han, Y. Yao, Z. Hadjri, J. Yang, J. Seo, L. Shi, S. Ye, K. Watanabe, T. Taniguchi, and L. Ju, Nature (London) **637**, 1090 (2025).
[35] A. Jahin and S.-Z. Lin, Phys. Rev. B **113**, 014504 (2026).
[36] M. Kim, A. Timmel, L. Ju, and X.-G. Wen, Phys. Rev. B **111**, 014508 (2025).
[37] Y.-Z. Chou, J. Zhu, and S. D. Sarma, Phys. Rev. B **111**, 174523 (2025).
[38] M. Geier, M. Davydova, and L. Fu, Nat. Commun. **17**, 232 (2026).
[39] H. Yang and Y.-H. Zhang, arXiv:2411.02503.
[40] Y.-Q. Wang, Z.-Q. Gao, and H. Yang, Phys. Rev. B **113**, 174507 (2026).
[41] Q. Qin and C. Wu, Chin. Phys. Lett. **43**, 030708 (2026).
[42] C. Yoon, T. Xu, Y. Barlas, and F. Zhang, Phys. Rev. Lett. **136**, 026603 (2026).
[43] G. Parra-Martinez, A. Jimeno-Pozo, V. T. Phong, H. Sainz-Cruz, D. Kaplan, P. Emanuel, Y. Oreg, P. A. Pantaleon, J. A. Silva-Guillen, and F. Guinea, Phys. Rev. Lett. **135**, 136503 (2025).
[44] H. Zhou, T. Xie, T. Taniguchi, K. Watanabe, and A. F. Young, Nature (London) **598**, 434 (2021).
[45] T. Han *et al.*, Nature (London) **643**, 654 (2025).
[46] M. Kumar, D. Waleffe, A. Okounkova, R. Tejani, V. T. Phong, K. Watanabe, T. Taniguchi, C. Lewandowski, J. Folk, and M. Yankowitz, arXiv:2507.18598.
[47] E. Morissette, P. Qin, H.-T. Wu, N. J. Zhang, R. Q. Nguyen, K. Watanabe, T. Taniguchi, and J. I. A. Li, arXiv:2504.05129.
[48] S. A. Murshed and B. Roy, Phys. Rev. B **112**, 085121 (2025).
[49] G. Jiang and Y. Barlas, Phys. Rev. Lett. **131**, 016002 (2023).
[50] G. D. Mahan, *Many-Particle Physics* (Plenum Press, New York, 1981), p. 1003.
[51] J. B. Ketterson and S. N. Song, *Superconductivity* (Cambridge University Press, Cambridge, England, 1999).
[52] P. Coleman, *Introduction to Many-Body Physics* (Cambridge University Press, Cambridge, England, 2015).
[53] E. Rossi, Curr. Opin. Solid State Mater. Sci. **25**, 100952 (2021).
[54] P. Törmä, S. Peotta, and B. A. Bernevig, Nat. Rev. Phys. **4**, 528 (2022).
[55] J. Yu, B. A. Bernevig, R. Queiroz, E. Rossi, P. Törmä, and B.-J. Yang, npj Quantum Mater. **10**, 101 (2025).
[56] F. Zhang, J. Jung, G. A. Fiete, Q. Niu, and A. H. MacDonald, Phys. Rev. Lett. **106**, 156801 (2011).
[57] B. Roy and I. F. Herbut, Phys. Rev. B **82**, 035429 (2010).
[58] From here onward, we use the term Haldane phase to refer to the QAH phase induced by the mass term $m\hat{\sigma}_z\tau_z$ in C2DEGs, even though the microscopic mechanism leading to this phase can vary depending on the chirality index J.
[59] In the minimal model of RG, the Chern number and chiral index correspond to the same integer J.
[60] H. Min and A. H. MacDonald, Phys. Rev. B **77**, 155416 (2008).
[61] H. Min, G. Borghi, M. Polini, and A. H. MacDonald, Phys. Rev. B **77**, 041407(R) (2008).
[62] F. Zhang, H. Min, M. Polini, and A. H. MacDonald, Phys. Rev. B **81**, 041402(R) (2010).
[63] F. R. Geisenhof, F. Winterer, A. M. Seiler, J. Lenz, T. Xu, F. Zhang, and R. T. Weitz, Nature (London) **598**, 53 (2021).
[64] F. Winterer, F. R. Geisenhof, N. Fernandez, A. M. Seiler, F. Zhang, and R. T. Weitz, Nat. Phys. **20**, 422 (2024).
[65] See Supplement Material at http://link.aps.org/supplemental/10.1103/k5r2-q11w for the calculation of the projected band pair susceptibility; for the estimates of the acoustic- and optical-mediated phonon pairing attraction; for the renormalization group analysis; for the details of the role of repulsive interactions; for the calculation of the superfluid density of the Kekulè superconducting state.
[66] C.-X. Liu, Y. Chen, A. Yazdani, and B. A. Bernevig, Phys. Rev. B **110**, 045133 (2024).
[67] We adopt a conservative estimate for the deformation field, noting that it can be up to twice as large [24,68]. A detailed study is required to determine different electron-phonon scattering processes that can contribute to the magnitude of the deformation field for each J-layer RG system.
[68] Y.-Z. Chou, F. Wu, J. D. Sau, and S. Das Sarma, Phys. Rev. Lett. **127**, 187001 (2021).
[69] K. P. Nuckolls, R. L. Lee, M. Oh, D. Wong, T. Soejima, J. P. Hong, D. Călugăru, J. Herzog-Arbeitman, B. A. Bernevig, K. Watanabe, T. Taniguchi, N. Regnault, M. P. Zaletel, and A. Yazdani, Nature (London) **620**, 525 (2023).
[70] C. Chen *et al.*, Nature (London) **636**, 342 (2024).
[71] J. P. L. Faye, M. N. Diarra, and D. Sénéchal, Phys. Rev. B **93**, 155149 (2016).
[72] F. Zhang, B. Sahu, H. Min, and A. H. MacDonald, Phys. Rev. B **82**, 035409 (2010).
[73] J. Martin, B. E. Feldman, R. T. Weitz, M. T. Allen, and A. Yacoby, Phys. Rev. Lett. **105**, 256806 (2010).
[74] F. Freitag, J. Trbovic, M. Weiss, and C. Schönenberger, Phys. Rev. Lett. **108**, 076602 (2012).
[75] V. N. Kotov, B. Uchoa, V. M. Pereira, F. Guinea, and A. H. Castro Neto, Rev. Mod. Phys. **84**, 1067 (2012).
[76] A. Himeda, T. Kato, and M. Ogata, Phys. Rev. Lett. **88**, 117001 (2002).
[77] F. Loder, A. P. Kampf, and T. Kopp, Phys. Rev. B **81**, 020511(R) (2010).
[78] P. A. Lee, Phys. Rev. X **4**, 031017 (2014).
[79] R. Soto-Garrido and E. Fradkin, Phys. Rev. B **89**, 165126 (2014).

[80] E. Fradkin, S. A. Kivelson, and J. M. Tranquada, Rev. Mod. Phys. **87**, 457 (2015).
[81] D. F. Agterberg, J. S. Davis, S. D. Edkins, E. Fradkin, D. J. Van Harlingen, S. A. Kivelson, P. A. Lee, L. Radzihovsky, J. M. Tranquada, and Y. Wang, Annu. Rev. Condens. Matter Phys. **11**, 231 (2020).
[82] Z. Han, S. A. Kivelson, and H. Yao, Phys. Rev. Lett. **125**, 167001 (2020).
[83] X. Liu, Y. X. Chong, R. Sharma, and J. C. S. Davis, Science **372**, 1447 (2021).
[84] E. Berg, E. Fradkin, E.-A. Kim, S. A. Kivelson, V. Oganesyan, J. M. Tranquada, and S. C. Zhang, Phys. Rev. Lett. **99**, 127003 (2007).
[85] D. F. Agterberg and H. Tsunetsugu, Nat. Phys. **4**, 639 (2008).
[86] E. Berg, E. Fradkin, S. A. Kivelson, and J. M. Tranquada, New J. Phys. **11**, 115004 (2009).
[87] D. F. Agterberg and J. Garaud, Phys. Rev. B **91**, 104512 (2015).
[88] Y. Wang, S. D. Edkins, M. H. Hamidian, J. C. Seamus Davis, E. Fradkin, and S. A. Kivelson, Phys. Rev. B **97**, 174510 (2018).
[89] Z. Dai, Y.-H. Zhang, T. Senthil, and P. A. Lee, Phys. Rev. B **97**, 174511 (2018).
[90] S. D. Edkins, A. Kostin, K. Fujita, A. P. Mackenzie, H. Eisaki, S. Uchida, S. Sachdev, M. J. Lawler, E.-A. Kim, J. C. S. Davis, and M. H. Hamidian, Science **364**, 976 (2019).
[91] D. F. Agterberg, M. Sigrist, and H. Tsunetsugu, Phys. Rev. Lett. **102**, 207004 (2009).
[92] S. Baruch and D. Orgad, Phys. Rev. B **77**, 174502 (2008).
[93] M. R. Norman and J. C. S. Davis, Proc. Natl. Acad. Sci. U.S.A. **115**, 5389 (2018).
[94] Here, we neglect coupling between the QAH and quantum valley Hall order parameters. Since our focus is on the role of nontrivial topology in the pair susceptibility, we consider the simpler case in which only one symmetry is broken at a time.
[95] T. O. Wehling, E. Şaşıoğlu, C. Friedrich, A. I. Lichtenstein, M. I. Katsnelson, and S. Blügel, Phys. Rev. Lett. **106**, 236805 (2011).
[96] G. Jiang and Y. Barlas, Phys. Rev. B **109**, 214518 (2024).
[97] X. Hu, E. Rossi, and Y. Barlas, Phys. Rev. B **112**, 144502 (2025).

End Matter

Interaction effects in J-layer RG—For long-range interactions that are both valley- and spin-independent, the spontaneously broken symmetry quantum valley Hall (QVH) and quantum anomalous Hall (QAH) phases are energetically degenerate. To distinguish between these competing states, one must consider interactions that break valley symmetry or differentiate between the sublattices. Since both QVH and QAH mass terms share the same sublattice structure but differ in their valley dependence, only valley-dependent interactions can lift their degeneracy. Therefore, we only include valley-dependent interactions in our analysis.

The interacting Hamiltonian, $H_{\rm int} = H_{ee} + H'_{\rm int}$, includes the SU(4) Coulomb interaction H_{ee}, with the Coulomb repulsion $v_{\mathbf{q}}$, and the valley-dependent interaction $H'_{\rm int}$

$$H_{\rm int} = \frac{1}{2L^2}\sum_{\mathbf{k},\mathbf{k}',\mathbf{q}} v_{\mathbf{q}} \psi^\dagger_{\mathbf{k}+\mathbf{q}}\psi_{\mathbf{k}}\psi^\dagger_{\mathbf{k}'-\mathbf{q}}\psi_{\mathbf{k}'} + \frac{1}{2L^2}\sum_{\mathbf{k},\mathbf{k}',\mathbf{q}}\sum_{\mu=z,x,y} u_\mu \psi^\dagger_{\mathbf{k}+\mathbf{q}}\hat{\tau}_\mu\psi_{\mathbf{k}}\psi^\dagger_{\mathbf{k}'-\mathbf{q}}\hat{\tau}_\mu\psi_{\mathbf{k}'}, \quad \text{(A1)}$$

where u_μ's are short-ranged valley-dependent interaction terms. $\hat{\tau}_z$ acts on the valley degree of freedom and L^2 denotes the sample area. For simplicity, we assume that $u_x = u_y = u_\perp$.

To perform the mean-field theory, we rewrite the Hamiltonian H by adding and subtracting the mean-field terms $H_{\hat{\Delta}}$ as $H = (H_0 + H_{\hat{\Delta}}) + (H_{\rm int} - H_{\hat{\Delta}}) = H_{\rm MF} + H_{\rm res}$, and H_0 corresponds to the noninteracting Hamiltonian. The mean-field Hamiltonian $H_{\rm MF}$ is treated as the nonperturbative Hamiltonian, and the effect of $H_{\rm res}$ can be studied via a diagrammatic approach. To ensure the field $\hat{\Delta}$ is self-consistently determined, we satisfy the tree-level self-consistent equation corresponding to the Feynman diagrams shown in Fig. 5. We consider the competition between interaction-induced mass terms, one corresponding to the QAH effect, m, and the other to the QVH effect, Δ. The QVH Hamiltonian $H_{\rm QVH} = \sum_{\mathbf{k}} \psi^\dagger_{\mathbf{k}}\Delta_{\rm VH}\hat{\sigma}_z\psi_{\mathbf{k}}$, and the QAH Hamiltonian as $H_{\rm QAH} = \sum_{\mathbf{k}} \psi^\dagger_{\mathbf{k}} m\hat{\sigma}_z\hat{\tau}_z\psi_{\mathbf{k}}$, where $\hat{\sigma}_z$ acts on the sublattice degree of freedom. In the presence of valley anisotropy, the self-consistent gap equation at the tree level becomes

$$\hat{\Delta} = -\frac{1}{\beta}\sum_n \int \frac{d^2k'}{(2\pi)^2}\left[v_{\mathbf{k}-\mathbf{k}'}G_{\rm MF}(\mathbf{k}', \iota\omega'_n) + \sum_{\mu=x,y,z} u_\mu\hat{\tau}_\mu G_{\rm MF}(\mathbf{k}', \iota\omega'_n)\hat{\tau}_\mu\right], \quad \text{(A2)}$$

where $G_{\rm MF}(\mathbf{k}) = [\iota\omega_n - H_{\rm MF}(\mathbf{k})]^{-1}$ is the Green's function associated with the mean-field Hamiltonian, $\omega_n = (2n+1)\pi/\beta$ and $\beta = 1/T$. Performing the summation over the frequencies, we arrive at the gap equations

$$m(\mathbf{k}) = \int \frac{d^2k'}{(2\pi)^2}\left[v_{\mathbf{k}-\mathbf{k}'} - 2u_\perp\right]\frac{m(\mathbf{k}')}{2E_{\mathbf{k}'}}\tanh\left(\frac{\beta E_{\mathbf{k}'}}{2}\right),$$
$$\Delta_{\rm VH}(\mathbf{k}) = \int \frac{d^2k'}{(2\pi)^2}\left[v_{\mathbf{k}-\mathbf{k}'} + 2u_\perp\right]\frac{\Delta_{VH}(\mathbf{k}')}{2E_{\mathbf{k}'}}\tanh\left(\frac{\beta E_{\mathbf{k}'}}{2}\right), \quad \text{(A3)}$$

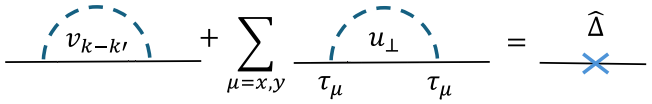


FIG. 5. Feynman diagram corresponding to the self-consistent solution to the gap equation for the mean field $\hat{\Delta}$.

where $E_{\mathbf{k}}^2 = |\epsilon_{J,\mathbf{k}}|^2 + m_{\mathbf{k}}^2$ for the QAH state, and $E_{\mathbf{k}}^2 = |\epsilon_{J,\mathbf{k}}|^2 + \Delta_{\mathrm{VH}}(\mathbf{k})^2$ for the QVH state [94]. From the structure of Eq. (A3), it is clear that only $u_\perp$ lifts the degeneracy of the QAH and QVH state; therefore, we take $u_z = 0$. The above equations imply that the QAH is preferred over the QVH state for $u_\perp < 0$. The negative sign that distinguishes the QAH state from the QVH state is due to the anticommutation of the Pauli matrices in the valley space $\hat{\tau}_z\hat{\tau}_x = -\hat{\tau}_x\hat{\tau}_z$ and $\hat{\tau}_z\hat{\tau}_y = -\hat{\tau}_y\hat{\tau}_z$.

Figure 6(a) shows the interaction-induced mass gaps as a function of the chirality index J for the bare Coulomb interaction $v_{\mathbf{q}} = 2\pi e^2/(\epsilon q)$ and $u_\perp < 0$ ($|u_\perp| \sim 2$ meV) computed for different values of the dielectric constant $\epsilon = 5$, 7.5, 10, 12.5, and 15. In the self-consistent calculation, we impose a momentum cutoff $k_c = \gamma_1/v$ and evaluate m at the Dirac point $\mathbf{k} = 0$. For low dielectric screening (e.g., $\epsilon = 5$), the interaction-induced mass gaps are substantial, with $m > 50$ meV. For reference, the dielectric constant of hBN is approximately $\epsilon \sim 6$. As expected, increasing the dielectric screening reduces the magnitude of the induced gaps. To account for the influence of nearby metallic gates, we incorporate a gate-screened Coulomb interaction $v_{\mathbf{q}}^{\mathrm{sc}} = v_{\mathbf{q}} \tanh(qd/2)$, where d is the distance between the gates. The results are plotted in Fig. 6(b). Even in the presence of gate screening, the mass gaps remain sizable for $\epsilon = 5$, particularly in tetra- and pentalayer graphene, where we find $m > 50$ meV.

Pair susceptibility in other channels—One can calculate the particle-particle susceptibility in the $\hat{\sigma}_z$ channel. Here, we restrict to even chiralities. Again estimating the leading logarithmic contribution one finds, $\Pi_{-S} = x^2\Pi_S$ and $\Pi_{-D} = (1-x^2)/2\Pi_S$, where $\Pi_{-S}(\Pi_{-D})$ are the inter- and intravalley pair susceptibility in the σ_z channel (Π_S denotes the even J intravalley pair susceptibility). The intravalley pair susceptibility exceeds the intervalley counterpart for $x > 1/\sqrt{3}$, indicating that in the $\hat{\sigma}_z$ channel intravalley Kekulé superconductivity should be favored when $\mu < \sqrt{3}m$. One can also evaluate the pair susceptibility in the $\hat{\sigma}_x$ and $\hat{\sigma}_y$ channels for the Haldane phase. Here, we find that the intervalley susceptibility dominates over the intravalley component. The channel dependence highlights the sensitivity of the pair susceptibility on the topological nature and the orbital character of the pairing interaction.

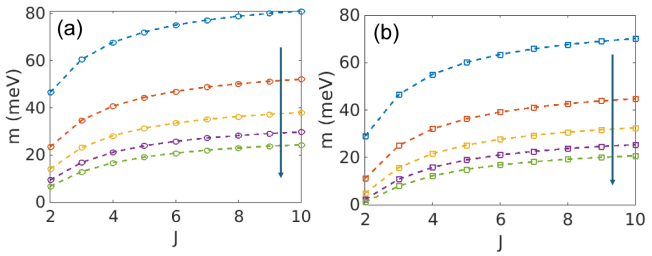


FIG. 6. Interaction-induced mass gaps for different chirality indices J for (a) long-range Coulomb interactions and (b) gate-screened interaction with $d = 10$ nm evaluated at the Dirac point with a cutoff $k_c = \gamma_1/(\hbar v)$. Each curve corresponds to a different value of the dielectric constant $\epsilon = 5$, 7.5, 10, 12.5, and 15, from the top to bottom, with an arrow indicating the direction of increasing ϵ.

Pair susceptibility in a displacement field—When inversion symmetry is explicitly broken, for example, by applying a finite displacement field ($\Delta_V \neq 0$), preserving the topological phase requires $\Delta_V < m$. Simultaneously, realizing two Fermi surfaces, where a distinction between inter- and intravalley pairing remains meaningful, necessitates $\Delta_V + m < \mu$. Defining $y = \Delta_V/\mu$, these constraints translate into the conditions $y < 1 - x$ and $y < x$. In this regime, the intravalley pair susceptibility becomes valley-dependent and is given by

$$\Pi_S(\pm 2\mathbf{K}_D) = \frac{N_0}{[1-(x\pm y)^2]^\alpha} \log\left(\frac{E_c}{T}\right) f_S(x \pm y) + \cdots. \tag{C1}$$

Meanwhile, the intervalley pair susceptibility loses its weak-coupling logarithmic divergence due to the breaking of inversion symmetry. Finally, in the limit $y > 1 - x$ and $y < x$, the system remains in the topological phase but hosts only a single Fermi surface at a single valley. This regime corresponds to a "quarter-metal" superconducting phase [42,48].

Electron repulsion—To account for the effect of electron repulsion, we project the nearest-neighbor repulsive interaction [95] onto the Fermi surface (see Supplemental Material [65]). Our calculations show that the intravalley nearest-neighbor projected interaction contains only an s-wave component. Therefore, for even chirality, the chiral-J Kekulé pairing interaction is unaffected by electron repulsion. In contrast, since the s-wave Kekulé state is influenced by the repulsive interaction, the corresponding phase boundary in Fig. 4(b) shifts toward higher carrier densities, with the phase transition depending on the magnitude of the repulsive interaction. A similar argument indicates that the phase boundary of the odd-chirality Kekulé superconductor will also shift to higher densities. Electron repulsion beyond nearest-neighbor interactions will also affect the critical temperature by reducing the effective pairing interaction. A quantitative

treatment of this effect requires an Eliashberg-type analysis, which is beyond the scope of the present work.

Critical temperature scaling—The critical temperature $T_c(x)$ for the even parity chiral-J Kekulé superconductor is determined by $g_{+,-J}$, whereas the s-wave Kekulé superconductor is determined by $g_{+,0}$. Figure 7(a) shows the behavior of $g_{+,-J}(g_{+,0})$ as a function of x for $J = 4$ and 6, with a Haldane mass $m = 10$ meV. Here, we use the effective pairing interaction $G_0 = 123$ meV nm^2, which ignores electron repulsion. As $x \to 1$, $g_{+,-J}$ increases sharply due to the large density of states at the bottom of the band, while $g_{+,0} \to 0$ due to suppression of the s-wave channel. At $x = 0.5$, we find $g_{0,-J} > g_{+,0}$, resulting in the s-wave Kekulé superconducting phase at higher densities. Using $\omega_D \sim 0.2$ eV and $g_{+,-J} \sim 0.1$–0.2, for $J = 4$, 6, yields $T_c^S \sim 90.8$ mK–13.5 K for the chiral-J Kekulé superconductor.

Superfluid stiffness—The superfluid stiffness of chiral 2DEGs, $\rho(m)$, contains both conventional and quantum-geometric contributions [96]. In the weak coupling limit, the stiffness is dominated by the conventional contribution, which is independent of Δ (see Supplemental Material [65]) [97]. For $m \neq 0$ and $\Delta/\mu_0 < 0.2$, where $\mu_0 = \sqrt{\mu^2 - m^2}$, we find

$$\rho(x) = \frac{J\zeta_J(2\pi n_e)^{J/2}}{\pi} h(x) = \rho_0 h(x), \tag{F1}$$

where $h(x)$ is a scaling function independent of both J and Δ. The geometric stiffness ρ_g scales as $\rho_g/\rho_0 \sim \Delta^2/(\mu^2 - m^2)$, therefore, in the weak-coupling limit it becomes negligible. This zero-temperature expression for stiffness is valid for both inter- and intravalley superconducting states and for any symmetry of the order parameter.

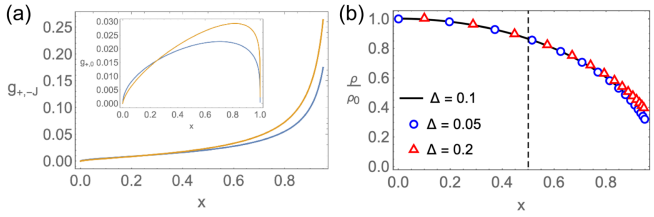


FIG. 7. (a) $g_{+,J}$ as a function of x for a Haldane mass $m = 10$ meV, for $J = 4$ and 6 in increasing order, with the inset corresponding to $g_{+,0}$. (b) Ratio of the superfluid stiffness ρ/ρ_0 as a function of x for a Haldane mass for $J = 4$ for different values of the order parameter $\Delta = 0.05$, 0.1, and 0.2 measured in units of $\mu_0 = (\mu^2 - m^2)^{1/2}$. The vertical dashed line denotes the phase transition from the s-wave Kekulé to the chiral-J Kekulé superconductor at $x = 1/2$.

For the Kekulé superconducting phase, $\rho(x)$ is shown as a function of x in Fig. 7(b). The results show that the stiffness is independent of the value of Δ in the weak-coupling limit. In the Kekulé superconducting state, which occurs at $x = 1/2$, the stiffness is approximately $\rho \approx 0.8\rho_0$. As x increases, the stiffness decreases to $\rho \approx 0.4\rho_0$ for $x \sim 0.95$, but it is still determined by the electron density n_e. As in a conventional two-dimensional electron gas, where Galilean invariance gives $\rho_s = \hbar^2 n_e/m^\star$, the superfluid stiffness in a chiral 2DEG with $\Delta \ll \mu$ is governed primarily by the carrier density $n_e^{J/2}$, with only weak dependence on the magnitude of the superconducting gap.

Supplemental Materials: Kekulé Superconductivity Induced by Quantum Geometry in Haldane Phases

Yafis Barlas,[1,*] Fan Zhang,[2] and Enrico Rossi[3]

[1]*Department of Physics, University of Nevada, Reno, Nevada 89557, USA*
[2]*Department of Physics, University of Texas at Dallas, Richardson, Texas 75080, USA*
[3]*Department of Physics, William and Mary, Williamsburg, Virginia 21387, USA*

CONTENTS

Pair susceptibility of Chiral 2DEGS in the Haldane Phase 2
Pair susceptibility of electrons in an Isolated Topological Band 2
Inter- and Intra-valley Pair susceptibility of a Haldane phase in a Chiral 2DEG 2
Spinless Chiral 2DEGs without a mass term 3
Odd chiraliy J 4
Even chiraliy J 4
Pair susceptibility for chiral 2DEGs with a Haldane mass 5
Odd chirality 5
Even chiraliy J 6

Density of states of Chiral 2DEGs 6

Longitudinal acoustic phonon-mediated pairing interactions in rhombohedral stacked graphene 7
Longitudinal acoustic phonons in rhombohedral stacked graphene 7
Electron-phonon coupling due to longitudinal acoustic phonons in rhombohedral stacked graphene 7
Estimates of the electron-phonon pairing attraction 8

Pairing Interaction in the Two-valley model 9
Intervalley Pairing Interaction 9
Intravalley Pairing Interaction 10
Decompsition into angular momentum channels (J = even) 11
Decompsition into angular momentum channels (J = odd) 12

Renormalization Groups Analysis of Kekulé Superconductivity in chiral 2DEGs 12
Superconducting instability for a single Fermi surface 12
Superconducting instability in chiral 2DEGs 13
Superconductivity for even chirality 15
Superconductivity for odd chirality 16

Effect of Electron repulsion on the Kekulé superconducting phase 17
Nearest neighbor repulsion 17

Superfluid stiffness of the Kekulé superconductor 19
Superfluid stiffness for $m = 0$ 19
Superfluid stiffness for $m \neq 0$ 20

References 21

PAIR SUSCEPTIBILITY OF CHIRAL 2DEGS IN THE HALDANE PHASE

In this section, we show that due to the topological nature of the chiral two-dimensional electron gas (C2DEG) in the Haldane phase, the intra-valley pair susceptibility dominates over the inter-valley pair susceptibility.

Pair susceptibility of electrons in an Isolated Topological Band

We start by calculating the pair susceptibility of electrons in an isolated spinless topological band. We assume that the Fermi energy lies within the conduction (valence) band and that the interaction strength $|U|$ is smaller than the Fermi energy μ (where μ is measured from the charge neutrality point $\mu = 0$), justifying projection onto the conduction (valence) band $\alpha = +(-)$. For explicit calculations, unless otherwise specified, we work exclusively in the conduction band. Particle-hole symmetry implies that the same results hold for the valence band. The finite-frequency Matsubara time particle-particle susceptibility, for an isolated α^{th} band with an orbital-dependent interaction *hat Lambda*, is given by

$$\Pi_\alpha(\mathbf{Q}, \imath\Omega) = \frac{1}{\beta}\sum_{\imath\omega}\int \frac{d^2\mathbf{k}}{(2\pi)^2}\mathrm{Tr}[\mathscr{G}_\alpha(\mathbf{k}+\mathbf{Q}, i\omega + i\Omega)\hat{\Lambda}\mathscr{G}_\alpha(-\mathbf{k}, -i\omega)\hat{\Lambda}], \tag{1}$$

where $\mathbf{Q}$ is the center-of-mass momentum of the Cooper pairs, Ω the frequency, $\mathscr{G}_\alpha(\mathbf{k}, i\omega)$ denotes the single-particle Green's function of the α^{th}-band given by

$$\mathscr{G}_\alpha(\mathbf{k}, i\omega) = \frac{|u_\alpha(\mathbf{k})\rangle\langle u_\alpha(\mathbf{k})|}{i\omega - \xi_{\mathbf{k}}} = \frac{P_\alpha(\mathbf{k})}{i\omega - \xi_{\alpha,\mathbf{k}}}, \tag{2}$$

and $\xi_{\alpha,\mathbf{k}} = \epsilon_{\alpha,\mathbf{k}} - \mu$, μ is the Fermi energy, $\epsilon_{\alpha,\mathbf{k}}$ is the energy of the α^{th}-band and $\hat{\Lambda}$ denotes the matrix in the orbital space. The Bloch wavefunction for the α^{th} band is denoted by $u_\alpha(\mathbf{k})$ and the projection operator of the α^{th}-band can be expressed as $P_\alpha(\mathbf{k}) = |u_\alpha(\mathbf{k})\rangle\langle u_\alpha(\mathbf{k})|$. Performing Matsubara summation using the contour method and taking the real part $\imath\Omega \to \Omega + \imath\eta$, the static pair susceptibility $\Omega = 0$ can be expressed as,

$$\Pi_\alpha(\mathbf{Q}) = \int \frac{d^2\mathbf{k}}{(2\pi)^2}\frac{1 - n_F(\xi_{\alpha,\mathbf{k}+\mathbf{Q}}) - n_F(\xi_{\alpha,-\mathbf{k}})}{\xi_{\alpha,\mathbf{k}+\mathbf{Q}} + \xi_{\alpha,-\mathbf{k}}}\mathrm{Tr}[P_\alpha(\mathbf{k}+\mathbf{Q})\hat{\Lambda}P_\alpha(-\mathbf{k})\hat{\Lambda}], \tag{3}$$

where $n_F(z)$ is the Fermi-Dirac distribution. For the two-band model, the projection operators for the $\alpha = \pm$ bands can be expressed as

$$P_\pm(\mathbf{k}) = \frac{\mathbb{I} \pm \hat{\sigma}\cdot\hat{\mathbf{h}}(\mathbf{k})}{2}, \tag{4}$$

where $\hat{\mathbf{h}}(\mathbf{k}) = \mathbf{h}(\mathbf{k})/|\mathbf{h}(\mathbf{k})|$ is the vector field associated with the Hamiltonian $H = \hat{\sigma}\cdot\hat{\mathbf{h}}(\mathbf{k})$ and $\epsilon(\pm, \mathbf{k}) = \pm|\mathbf{h}(\mathbf{k})|$. Therefore the band projected pair susceptibility for the α^{th}-band for $\hat{\Lambda} = \mathbb{I}$ can be expressed as

$$\Pi_\pm(\mathbf{Q}) = \int \frac{d^2\mathbf{k}}{(2\pi)^2}\frac{1 - n_F(\xi_\pm(\mathbf{k}+\mathbf{Q})) - n_F(\xi_\pm(-\mathbf{k}))}{\xi_\pm(\mathbf{k}+\mathbf{Q}) + \xi_\pm(-\mathbf{k})}\Big(\frac{1 + \hat{\mathbf{h}}_{\mathbf{k}+\mathbf{Q}}\cdot\hat{\mathbf{h}}_{-\mathbf{k}}}{2}\Big). \tag{5}$$

Inter- and Intra-valley Pair susceptibility of a Haldane phase in a Chiral 2DEG

We now specialize to the conduction band $\alpha = +$ of the chiral two-dimensional electron gas (C2DEG) in the Haldane phase. The Haldane mass term obeys inversion symmetry, $\epsilon(\alpha, \mathbf{k}) = \epsilon(\alpha, -\mathbf{k})$, where $\mathbf{k}$ is defined over the Brillouin zone (BZ). For densities between one-quarter and three-quarters filling of the BZ, rhombohedral graphene exhibits two Fermi valleys at each Dirac point. For two-Fermi valleys, one each at the Dirac points, there are two possible nesting scenarios: i) inter-valley pairing and ii) intra-valley pairing (see Fig. 1).

We take the M point of the BZ at the origin, with the Dirac points at $\mathbf{K}_D = (2\pi/3, 0)$ and $\mathbf{K}' = -\mathbf{K}_D = (-2\pi/3, 0)$, as indicated in Fig. 1. We start with the intra-valley pair susceptibility at $-\mathbf{K}_D$. Take $\mathbf{k} = \mathbf{K}_D + \mathbf{p}$ ($\mathbf{p}$ is the momentum measured at either Dirac point), giving $-\mathbf{k} = -\mathbf{K}_D - \mathbf{p}$ and $\mathbf{k} + \mathbf{Q} = \mathbf{K}_D + \mathbf{p} + \mathbf{Q}$. For the intra-valley pair susceptibility at $\mathbf{K}_D$, we take $\mathbf{k} = -\mathbf{K}_D + \mathbf{p}$ ($\mathbf{p}$ is the momentum measured at either Dirac point), giving $-\mathbf{k} = \mathbf{K}_D - \mathbf{p}$ and $\mathbf{k} + \mathbf{Q} = -\mathbf{K}_D + \mathbf{p} + \mathbf{Q}$. It is then easy to see that $\Pi(\mathbf{q}, 2\mathbf{K}_D) = \Pi(\mathbf{q}, -2\mathbf{K}_D) = \Pi_S(\mathbf{q})$, where Π_S denotes the intra-valley pair susceptibility. The intra-valley pair susceptibility $\Pi_S(\mathbf{q})$ is given by,

$$\Pi(\mathbf{q}, \pm 2\mathbf{K}_D) = \Pi_S(\mathbf{q}) = \int \frac{d^2\mathbf{p}}{(2\pi)^2}\frac{1 - n_F(\xi_{\pm\mathbf{K}_D}(\mathbf{p}+\mathbf{q})) - n_F(\xi_{\pm\mathbf{K}_D}(-\mathbf{p}))}{\xi_{\pm\mathbf{K}_D}(\mathbf{p}+\mathbf{q}) + \xi_{\pm\mathbf{K}_D}(-\mathbf{p})}\Big(\frac{1}{2}(1 + \hat{\mathbf{h}}_{\pm\mathbf{K}_D}(\mathbf{p})\cdot\hat{\mathbf{h}}_{\pm\mathbf{K}_D}(-\mathbf{p}))\Big). \tag{6}$$

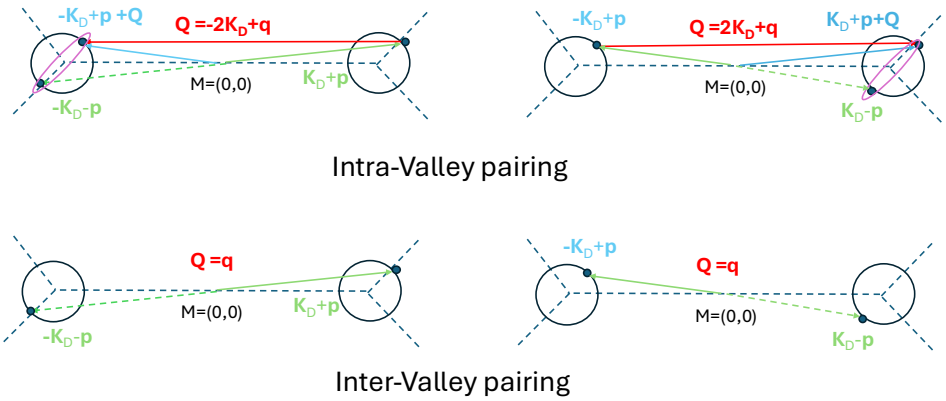


FIG. 1: The intra- and inter-valley pair susceptibility for the two-valley model of rhombohedral stacked multi-layer graphene.

Since we are working with a continuum approximation for a dispersive band, the integral over the momentum $\mathbf{p}$ is taken at the respective Dirac point $\mathbf{K}_D(-\mathbf{K}_D)$, with a cutoff in momentum space $\Lambda \sim 1/a_0$. The intra-valley pair susceptibility corresponds to the momenta $\mathbf{p}$ and $\mathbf{p}+\mathbf{q}$ belonging to the same valley (either at $\mathbf{K}_D$ or $-\mathbf{K}_D$). Due to nesting at the Fermi surface, a weak-coupling logarithmic instability arises, requiring an energy cutoff E_c.

The inter-valley pair susceptibility can be calculated by taking $\mathbf{k} = \mathbf{K}_D + \mathbf{p}$ ($\mathbf{p}$ is the momentum measured at either Dirac point), giving $-\mathbf{k} = -\mathbf{K}_D - \mathbf{p}$ and $\mathbf{k}+\mathbf{Q} = \mathbf{K}_D + \mathbf{p} + \mathbf{Q}$. The inter-valley pair susceptibility corresponds to $\mathbf{p}$ and $\mathbf{p}+\mathbf{q}$ belonging to different Fermi valleys. For the other contribution to the inter-valley pair susceptibility, take $\mathbf{k} = -\mathbf{K}_D + \mathbf{p}$ ($\mathbf{p}$ is the momentum measured at either Dirac point), giving $-\mathbf{k} = \mathbf{K}_D - \mathbf{p}$ and $\mathbf{k}+\mathbf{Q} = -\mathbf{K}_D + \mathbf{p} + \mathbf{Q}$. The inter-valley pair susceptibility is

$$\Pi(\mathbf{q}, \mathbf{Q}=0) = \Pi_D(\mathbf{q}) = \int \frac{d^2\mathbf{p}}{(2\pi)^2} \frac{1 - n_F(\xi_{\mathbf{K}_D}(\mathbf{p}+\mathbf{q})) - n_F(\xi_{-\mathbf{K}_D}(-\mathbf{p}))}{\xi_{\mathbf{K}_D}(\mathbf{p}+\mathbf{q}) + \xi_{-\mathbf{K}_D}(-\mathbf{p})} \Big(\frac{1}{2}(1 + \hat{\mathbf{h}}_{\mathbf{K}_D}(\mathbf{p}) \cdot \hat{\mathbf{h}}_{-\mathbf{K}_D}(-\mathbf{p}))\Big). \tag{7}$$

While the choice of the M point as the origin is not standard, it doesn't change the physics. One could have easily choosen the Γ point as the origin in which case the momentum transfer $\mathbf{Q} = (8\pi/3, 0)$ or $\mathbf{Q} = (-8\pi/3, 0)$, but since $(8\pi/3, 0) = \mathbf{b}_1 + \mathbf{K}_D = (-4\pi/3, 0)$ and $(-8\pi/3, 0) = -\mathbf{b}_1 - \mathbf{K}_D = (4\pi/3, 0)$, where $\mathbf{b}_1 = (2\pi, 0)$, these definitions only defer by a lattice vector and

$$(8\pi/3, 0) \equiv (-4\pi/3, 0); \qquad (-8\pi/3, 0) \equiv (4\pi/3, 0). \tag{8}$$

Spinless Chiral 2DEGs without a mass term

We first study the case of chiral-J 2DEGs without a mass term. As indicated in Fig. 2, for the intra-valley pairing, the spinor structure on a spinless Fermi surface is essential for the determination of the pair susceptibility. In the case of odd chirality, the spinor rotates an odd number of times, $= J\pi = (2n+1)\,pi$, when the particle on the Fermi surface traverses by π (see Fig. 2 a). Consequently, the spinors at the opposite sides of the Fermi surface are anti-parallel, corresponding to $\hat{\mathbf{h}}_{\mathbf{p}} \cdot \hat{\mathbf{h}}_{-\mathbf{p}} = -1$, resulting in the destructive interference and cancellation of the coherence factors. Alternatively for even chrality, the spinor rotates and even number of times $= J\pi = 2n\pi$ times when the particle on the Fermi surface traverses by π(see Fig. 2 b). Consequently, the spinors at the opposite sides of the Fermi surface are parallel, corresponding to $\hat{\mathbf{h}}_{\mathbf{p}} \cdot \hat{\mathbf{h}}_{-\mathbf{p}} = 1$, resulting in constructive interference and an addition of the coherence factors. As a reference, we plot the spinor structure of the helical Rashba gas, which shares the same phenomenological pairing behavior at zero magnetic fields.

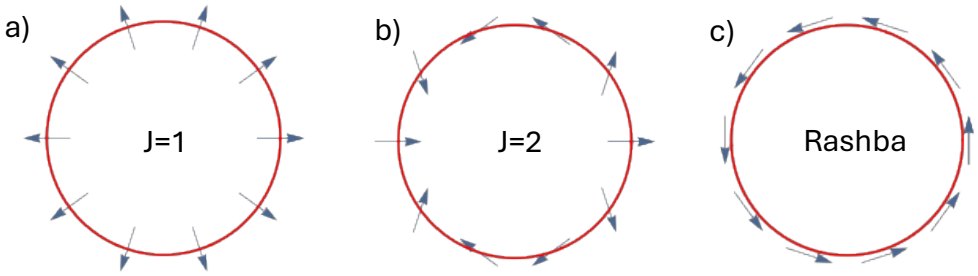


FIG. 2: Graphene (a), bilayer graphene (b), and Rashba (c) spinor on the Fermi surface. In graphene ($J = 1$), the pseudo-spinors at opposite sides of the Fermi surface at $\mathbf{p}$ and $-\mathbf{p}$ are anti-parallel, resulting in band geometry-induced destructive interference, while for bilayer graphene ($J = 2$), the pseudo-spinors at $\mathbf{p}$ and $-\mathbf{p}$ are parallel, resulting in constructive interference. Even though the spinor structure in the Rashba case is different from $J = 1$, the spinors at opposite sides of the Fermi surface are anti-parallel, giving the same phenomenology as graphene.

Odd chiraliy J

The Hamiltonian for a chiral-J2DEG without a mass term can be expressed as

$$H = \xi_J p^J \Big(\sigma_x \cos(J\varphi_{\mathbf{p}}) + \tau_z \sigma_y \sin(J\varphi_{\mathbf{p}}) \Big). \tag{9}$$

The spinor field for the chiral-J 2DEG at the Dirac points can be expressed as,

$$\hat{\mathbf{h}}_{\mathbf{K}_D}(\mathbf{p}) = (\cos(J\varphi_{\mathbf{p}}), \sin(J\varphi_{\mathbf{p}}), 0), \quad \hat{\mathbf{h}}_{-\mathbf{K}_D}(\mathbf{p}) = (\cos(J\varphi_{\mathbf{p}}), -\sin(J\varphi_{\mathbf{p}}), 0). \tag{10}$$

The $-\mathbf{p}$ spinor corresponds to $\varphi_{-\mathbf{p}} = \varphi_{\mathbf{p}} + \pi$. For odd values of J this becomes,

$$\hat{\mathbf{h}}_{\mathbf{K}_D}(-\mathbf{p}) = (-\cos(J\varphi_{\mathbf{p}}), -\sin(J\varphi_{\mathbf{p}}), 0), \quad \hat{\mathbf{h}}_{-\mathbf{K}_D}(-\mathbf{p}) = (-\cos(J\varphi_{\mathbf{p}}), \sin(J\varphi_{\mathbf{p}}), 0). \tag{11}$$

Since the pseudospinors in the same valley at the opposite sides of the Fermi surface point in opposite directions or are anti-parallel, for the intra-valley pairing we get $\hat{\mathbf{h}}_{\mathbf{K}_D}(\mathbf{p}) \cdot \hat{\mathbf{h}}_{\mathbf{K}_D}(-\mathbf{p}) = -1$. The coherence factors for intra-valley pairing become,

$$\frac{1}{2}(1 + \hat{\mathbf{h}}_{\mathbf{K}_D}(\mathbf{p}) \cdot \hat{\mathbf{h}}_{\mathbf{K}_D}(-\mathbf{p})) = \frac{1}{2}(1 + \hat{\mathbf{h}}_{-\mathbf{K}_D}(\mathbf{p}) \cdot \hat{\mathbf{h}}_{-\mathbf{K}_D}(-\mathbf{p})) = \frac{1}{2}(1 - (\cos^2 J\varphi_{\mathbf{p}} + \sin^2 J\varphi_{\mathbf{p}})) = 0. \tag{12}$$

For the inter-valley pairing,

$$\frac{1}{2}(1 + \hat{\mathbf{h}}_{\mathbf{K}_D}(\mathbf{p}) \cdot \hat{\mathbf{h}}_{-\mathbf{K}_D}(-\mathbf{p})) = \frac{1}{2}(1 + \hat{\mathbf{h}}_{-\mathbf{K}_D}(\mathbf{p}) \cdot \hat{\mathbf{h}}_{\mathbf{K}_D}(-\mathbf{p})) = \frac{1}{2}(1 - (\cos^2 J\varphi_{\mathbf{p}} - \sin^2 J\varphi_{\mathbf{p}})) = \frac{1}{2}(1 - \cos 2J\varphi_{\mathbf{p}}). \tag{13}$$

For odd chirality without a mass term, the inter- and intra-valley pair susceptibility for the conduction band, denoted by Π_S and Π_D, can now be easily calculated, giving

$$\Pi_S = 0, \qquad \Pi_D = \frac{N(0)}{2} \log\left(\frac{E_c}{k_\beta T}\right) + \cdots, \tag{14}$$

where $\cdots$ denote the regular terms and $N(0)$ denotes the density of states at the Fermi level.

Even chiraliy J

The spinor field for the chiral-J 2DEG at the Dirac points can be expressed as,

$$\hat{\mathbf{h}}_{\mathbf{K}_D}(\mathbf{p}) = (\cos(J\varphi_{\mathbf{p}}), \sin(J\varphi_{\mathbf{p}}), 0), \quad \hat{\mathbf{h}}_{-\mathbf{K}_D}(\mathbf{p}) = (\cos(J\varphi_{\mathbf{p}}), -\sin(J\varphi_{\mathbf{p}}), 0). \tag{15}$$

The $-\mathbf{p}$ spinor corresponds to $\varphi_{-\mathbf{p}} = \varphi_{\mathbf{p}} + \pi$. For even values of J this becomes,

$$\hat{\mathbf{h}}_{\mathbf{K}_D}(-\mathbf{p}) = (\cos(J\varphi_{\mathbf{p}}), \sin(J\varphi_{\mathbf{p}}), 0), \quad \hat{\mathbf{h}}_{-\mathbf{K}_D}(-\mathbf{p}) = (\cos(J\varphi_{\mathbf{p}}), -\sin(J\varphi_{\mathbf{p}}), 0). \tag{16}$$

Since the pseudospinors in the same valley at the opposite sides of the Fermi surface point in the same direction or are parallel, for the intra-valley pairing we get $\hat{\mathbf{h}}_{\mathbf{K}_D}(\mathbf{p}) \cdot \hat{\mathbf{h}}_{\mathbf{K}_D}(-\mathbf{p}) = 1$. Therefore, the coherence factors for intra-valley pairing are

$$\frac{1}{2}(1 + \hat{\mathbf{h}}_{\mathbf{K}_D}(\mathbf{p}) \cdot \hat{\mathbf{h}}_{\mathbf{K}_D}(-\mathbf{p})) = \frac{1}{2}(1 + \hat{\mathbf{h}}_{-\mathbf{K}_D}(\mathbf{p}) \cdot \hat{\mathbf{h}}_{-\mathbf{K}_D}(-\mathbf{p})) = \frac{1}{2}(1 + (\cos^2 J\varphi_{\mathbf{p}} + \sin^2 J\varphi_{\mathbf{p}})) = 1. \tag{17}$$

For the inter-valley pairing one has the factors,

$$\frac{1}{2}(1 + \hat{\mathbf{h}}_{\mathbf{K}_D}(\mathbf{p}) \cdot \hat{\mathbf{h}}_{-\mathbf{K}_D}(-\mathbf{p})) = \frac{1}{2}(1 + \hat{\mathbf{h}}_{-\mathbf{K}_D}(\mathbf{p}) \cdot \hat{\mathbf{h}}_{\mathbf{K}_D}(-\mathbf{p})) = \frac{1}{2}(1 - (\cos^2 J\varphi_{\mathbf{p}} - \sin^2 J\varphi_{\mathbf{p}})) = \frac{1}{2}(1 + \cos 2J\varphi_{\mathbf{p}}). \tag{18}$$

For even chirality without a mass term, the inter- and intra-valley pair susceptibility for the conduction band, denoted by Π_S and Π_D, can now be easily calculated, giving

$$\Pi_S = N(0) \log\left(\frac{E_c}{k_\beta T}\right) + \cdots, \qquad \Pi_D = \frac{N(0)}{2} \log\left(\frac{E_c}{k_\beta T}\right) + \cdots, \tag{19}$$

where $\cdots$ denote the regular terms and $N(0)$ denotes the density of states at the Fermi level. From the above calculation, we see that the inter- and intra-valley pair susceptibilities depend strongly on the parity of the chiral index. Next, we consider the case of a topological mass term on the inter- and intra-valley pair susceptibilities in chiral 2DEGs.

Pair susceptibility for chiral 2DEGs with a Haldane mass

We now move to the case of a chiral-J Hamiltonian with a Haldane mass term, which can be expressed as

$$H = \xi_J p^J \Big(\sigma_x \cos(J\varphi_{\mathbf{p}}) + \tau_z \sigma_y \sin(J\varphi_{\mathbf{p}})\Big) + m\sigma_z\tau_z. \tag{20}$$

Odd chirality

Defining $\cos(\theta_{\mathbf{p}}) = m/\epsilon_{\mathbf{p}}$, the spinor field for the chiral-J 2DEG at the Dirac points can be expressed as,

$$\hat{\mathbf{h}}_{\mathbf{K}_D}(\mathbf{p}) = (\sin(\theta_{\mathbf{p}})\cos(J\varphi_{\mathbf{p}}), \sin(\theta_{\mathbf{p}})\sin(J\varphi_{\mathbf{p}}), \cos(\theta_{\mathbf{p}})), \quad \hat{\mathbf{h}}_{-\mathbf{K}_D}(\mathbf{p}) = (\sin(\theta_{\mathbf{p}})\cos(J\varphi_{\mathbf{p}}), -\sin(\theta_{\mathbf{p}})\sin(J\varphi_{\mathbf{p}}), -\cos(\theta_{\mathbf{p}})). \tag{21}$$

The $-\mathbf{p}$ spinor corresponds to $\varphi_{-\mathbf{p}} = \varphi_{\mathbf{p}} + \pi$. For odd values of J this becomes,

$$\hat{\mathbf{h}}_{\mathbf{K}_D}(-\mathbf{p}) = (-\sin(\theta_{\mathbf{p}})\cos(J\varphi_{\mathbf{p}}), -\sin(\theta_{\mathbf{p}})\sin(J\varphi_{\mathbf{p}}), \cos(\theta_{\mathbf{p}})), \quad \hat{\mathbf{h}}_{-\mathbf{K}_D}(-\mathbf{p}) = (-\sin(\theta_{\mathbf{p}})\cos(J\varphi_{\mathbf{p}}), \sin(\theta_{\mathbf{p}})\sin(J\varphi_{\mathbf{p}}), -\cos(\theta_{\mathbf{p}})). \tag{22}$$

In the presence of a Haldane mass term, the coherence factors for intra-valley pairing are

$$\frac{1}{2}(1 + \hat{\mathbf{h}}_{\mathbf{K}_D}(\mathbf{p}) \cdot \hat{\mathbf{h}}_{\mathbf{K}_D}(-\mathbf{p})) = \frac{1}{2}(1 + \hat{\mathbf{h}}_{-\mathbf{K}_D}(\mathbf{p}) \cdot \hat{\mathbf{h}}_{-\mathbf{K}_D}(-\mathbf{p})) = \frac{1}{2}(1 - \sin^2(\theta_{\mathbf{p}})(\cos^2 J\varphi_{\mathbf{p}} + \sin^2 J\varphi_{\mathbf{p}}) + \cos^2(\theta_{\mathbf{p}})) \tag{23}$$

$$= \frac{1}{2}(1 + (\cos^2(\theta_{\mathbf{p}}) - \sin^2(\theta_{\mathbf{p}}))) = \cos^2(\theta_{\mathbf{p}}) = \left(\frac{m}{\epsilon_{\mathbf{p}}}\right)^2. \tag{24}$$

For the inter-valley pairing, the coherence factors are,

$$\frac{1}{2}(1 + \hat{\mathbf{h}}_{\mathbf{K}_D}(\mathbf{p}) \cdot \hat{\mathbf{h}}_{-\mathbf{K}_D}(-\mathbf{p})) = \frac{1}{2}(1 + \hat{\mathbf{h}}_{-\mathbf{K}_D}(\mathbf{p}) \cdot \hat{\mathbf{h}}_{\mathbf{K}_D}(-\mathbf{p})) = \frac{1}{2}(1 - \sin^2(\theta_{\mathbf{p}})(\cos^2 J\varphi_{\mathbf{p}} - \sin^2 J\varphi_{\mathbf{p}}) - \cos^2(\theta_{\mathbf{p}})) \tag{25}$$

$$= \frac{1}{2}(1 - \cos^2(\theta_{\mathbf{p}}) - \sin^2(\theta_{\mathbf{p}})\cos 2J\varphi_{\mathbf{p}}). \tag{26}$$

For odd chirality with a Haldane mass term, the inter- and intra-valley pair susceptibility for the conduction band, denoted by Π_S and Π_D, can now be easily calculated, giving

$$\Pi_S = N(0) \log\left(\frac{E_c}{k_\beta T}\right) x^2 + \cdots, \qquad \Pi_D = N(0) \log\left(\frac{E_c}{k_\beta T}\right) \frac{1 - x^2}{2} + \cdots, \tag{27}$$

where $x = m/\mu$, where μ denotes the Fermi energy, $\cdots$ denote the regular terms and $N(0)$ denotes the density of states at the Fermi level.

Even chiraliy J

The spinor field for the chiral-J 2DEG at the Dirac points can be expressed as,

$$\hat{\mathbf{h}}_{\mathbf{K}_D}(\mathbf{p}) = (\sin(\theta_\mathbf{p})\cos(J\varphi_\mathbf{p}), \sin(\theta_\mathbf{p})\sin(J\varphi_\mathbf{p}), \cos(\theta_\mathbf{p})), \quad \hat{\mathbf{h}}_{-\mathbf{K}_D}(\mathbf{p}) = (\sin(\theta_\mathbf{p})\cos(J\varphi_\mathbf{p}), -\sin(\theta_\mathbf{p})\sin(J\varphi_\mathbf{p}), -\cos(\theta_\mathbf{p})). \quad (28)$$

The $-\mathbf{p}$ spinor, corresponds to $\varphi_{-\mathbf{p}} = \varphi_\mathbf{p} + \pi$. For even values of J this becomes,

$$\hat{\mathbf{h}}_{\mathbf{K}_D}(-\mathbf{p}) = (\sin(\theta_\mathbf{p})\cos(J\varphi_\mathbf{p}), \sin(\theta_\mathbf{p})\sin(J\varphi_\mathbf{p}), \cos(\theta_\mathbf{p})), \quad \hat{\mathbf{h}}_{-\mathbf{K}_D}(-\mathbf{p}) = (\sin(\theta_\mathbf{p})\cos(J\varphi_\mathbf{p}), -\sin(\theta_\mathbf{p})\sin(J\varphi_\mathbf{p}), -\cos(\theta_\mathbf{p})). \quad (29)$$

In the presence of a Haldane mass, the coherence factors for intra-valley pairing are

$$\frac{1}{2}(1 + \hat{\mathbf{h}}_{\mathbf{K}_D}(\mathbf{p}) \cdot \hat{\mathbf{h}}_{\mathbf{K}_D}(-\mathbf{p})) = \frac{1}{2}(1 + \hat{\mathbf{h}}_{-\mathbf{K}_D}(\mathbf{p}) \cdot \hat{\mathbf{h}}_{-\mathbf{K}_D}(-\mathbf{p})) = \frac{1}{2}(1 + \sin^2(\theta_\mathbf{p})(\cos^2 J\varphi_\mathbf{p} + \sin^2 J\varphi_\mathbf{p}) + \cos^2(\theta_\mathbf{p})) = 1. \quad (30)$$

For the inter-valley pairing,

$$\frac{1}{2}(1 + \hat{\mathbf{h}}_{\mathbf{K}_D}(\mathbf{p}) \cdot \hat{\mathbf{h}}_{-\mathbf{K}_D}(-\mathbf{p})) = \frac{1}{2}(1 + \hat{\mathbf{h}}_{-\mathbf{K}_D}(\mathbf{p}) \cdot \hat{\mathbf{h}}_{\mathbf{K}_D}(-\mathbf{p})) = \frac{1}{2}(1 - \sin^2(\theta_\mathbf{p})(\cos^2 J\varphi_\mathbf{p} - \sin^2 J\varphi_\mathbf{p}) - \cos^2(\theta_\mathbf{p})) \quad (31)$$

$$= \frac{1}{2}(1 + \sin^2(\theta_\mathbf{p})\cos 2J\varphi_\mathbf{p} - \cos^2(\theta_\mathbf{p})). \quad (32)$$

For even chiral with a Haldane mass, the inter- and intra-valley pair susceptibility for the conduction band, denoted by Π_S and Π_D, can now be easily calculated, giving

$$\Pi_S = N(0)\log\left(\frac{E_c}{k_\beta T}\right) + \cdots, \qquad \Pi_D = N(0)\log\left(\frac{E_c}{k_\beta T}\right)\frac{1-x^2}{2} + \cdots, \quad (33)$$

where $x = m/\mu$, where μ denotes the Fermi energy, $\cdots$ denote the regular terms and $N(0)$ denotes the density of states at the Fermi level.

DENSITY OF STATES OF CHIRAL 2DEGS

The energy dispersion in a chiral 2DEGs is gets gapped by a mass term m, which can be expressed as $\epsilon_\mathbf{k} = (\zeta_J^2 k^{2J} + m^2)^{1/2}$ with $\zeta_J = (\hbar v)^2/\gamma_1$. The density of states can be expressed as,

$$D(\epsilon) = \int \frac{d^2k}{(2\pi)^2}\delta((\zeta_J^2 k^{2J} + m^2)^{1/2} - \epsilon) = \int \frac{kdk}{2\pi}\delta((\zeta_J^2 k^{2J} + m^2)^{1/2} - \epsilon). \quad (34)$$

Making the substitution $u^2 = \zeta_J^2 k^{2J} + m^2$ we can write

$$udu = J\zeta_J^2 k^{2J-1}dk \qquad \Longrightarrow \qquad kdk = \frac{udu}{J\zeta_J^2 k^{2J-2}}, \quad (35)$$

which on inverting $u^2 = \zeta_J^2 k^{2J} + m^2$ and substitution of

$$k = \left(\frac{u^2 - m^2}{\zeta_J^2}\right)^{1/2J} \qquad \Longrightarrow \qquad \frac{1}{k^{2J-2}} = \left(\frac{\zeta_J^2}{u^2 - m^2}\right)^\alpha \quad (36)$$

where $\alpha = (2J-2)/(2J)$, gives us

$$D(\epsilon) = \frac{1}{2\pi J\zeta_J^{2-2\alpha}}\int_m^\infty du\frac{u}{(u^2-m^2)^\alpha}\delta(u-\epsilon) = \frac{1}{2\pi J\zeta_J^{2-2\alpha}}\frac{\epsilon}{(\epsilon^2-m^2)^\alpha}\theta(\epsilon - m). \quad (37)$$

We confirm this has the correct dimension for the density of states $[D(\epsilon)] = E^{-1}A^{-1}$, where E denotes energy and $A = L^2$, and L is the length. Using the fact that $[\zeta_J] = EL^J$ we can write

$$[D(\epsilon)] = E^{2\alpha-2}E^1E^{-2\alpha}(L^{-J})^{2-2\alpha} = E^{2\alpha-2+1-2\alpha}L^{2J(\alpha-1)} = E^{-1}L^{-2} \quad (38)$$

It is convenient to scale all the energies by the Fermi energy (chemical potential) μ and express the density of states as,

$$D(\epsilon) = \frac{1}{2\pi J\zeta_J^{2-2\alpha}\mu^{2\alpha-1}}\frac{\tilde{\epsilon}}{(\tilde{\epsilon}^2-\tilde{m}^2)^\alpha}\theta(\tilde{\epsilon}-\tilde{m}) = N_0\frac{\tilde{\epsilon}}{(\tilde{\epsilon}^2-\tilde{m}^2)^\alpha}\theta(\tilde{\epsilon}-\tilde{m}). \quad (39)$$

Using $\alpha = 1 - 1/J$ we can define $\beta = 2 - 2\alpha = 2/J$, giving us $2\alpha - 1 = 1 - \beta$, we can write

$$N_0 = \frac{1}{2\pi J \zeta_J^{\beta} \mu^{1-\beta}}. \tag{40}$$

Using this, we can express the density of states for the Hamiltonian

$$H_J(\tau_z, \mathbf{p}) = \zeta_J |\mathbf{p}|^J (\hat{\sigma}_x \cos(J\varphi_{\mathbf{p}}) + \tau_z \hat{\sigma}_y \sin(J\varphi_{\mathbf{p}})) + m\hat{\sigma}_z\tau_z + \Delta_V \hat{\sigma}_z, \tag{41}$$

in each valley $\tau_z = \pm 1$ can be expressed as

$$D_{\tau_z}(\epsilon) = \frac{1}{2\pi J \zeta_J^{2-2\alpha}} \frac{\epsilon}{(\epsilon^2 - (m + \tau_z\Delta_V)^2)^{\alpha}} \theta(\epsilon - (m + \tau_z\Delta_V)), \tag{42}$$

with $\alpha = 1 - 1/J$ and $\beta = 2 - 2\alpha = 2/J$.

LONGITUDINAL ACOUSTIC PHONON-MEDIATED PAIRING INTERACTIONS IN RHOMBOHEDRAL STACKED GRAPHENE

Longitudinal acoustic phonons in rhombohedral stacked graphene

The longitudinal acoustic phonons in graphene correspond to the in-phase motion of the Carbon atoms in the unit cell, within the projected two-dimensional plane. In the rhombohedral stacked graphene, distinct oscillations in the middle layers contribute to the in-plane and out-of-plane motion of the projected sublattices. The number of possible oscillations that lead to the in-phase or out-of-phase motion of the low-energy unstacked Carbon atoms $(1A, JB)$ depends on the number of layers. Therefore, to distinguish these modes from the longitudinal acoustic (LA) and longitudinal optical (LO) modes of the graphene, the in-phase motion of the stacked Carbon atoms $(1A, JB)$ will henceforth be called the LA' mode, while the out-of-phase motion of the stacked Carbon atoms $(1A, NB)$ will be called the LO' mode. For a J-layer RG stack, there are a total of 2^{J-1} distinct lattice oscillations that contribute to the LA' phonon mode and 2^{J-1} distinct lattice oscillations that contribute to the LO' phonon modes.

Electron-phonon coupling due to longitudinal acoustic phonons in rhombohedral stacked graphene

We now consider out-of-plane LA' phonon-mediated pairing attraction on a rhombohedral graphene lattice, corresponding to a two-orbital projected lattice with the orbitals $\alpha, \beta = 1A, JB$, where J denotes the number of layers. We assume that inter-layer phonon coupling is weak, and express the continuum limit of the electron-phonon coupling (EPC) Hamiltonian as,

$$H_{EPC} = D \int d\mathbf{r} \nabla U(\mathbf{r}) \sum_{\sigma = 1A, JB} \psi^{\dagger}_{\sigma}(\mathbf{r}) \psi_{\sigma}(\mathbf{r}), \tag{43}$$

where $D \sim 15$ eV is the effective deformation potential and $U(\mathbf{r})$ is the deformation field [1, 2]. To proceed, we move to momentum space, quantize the deformation potential in terms of bosonic operators $b_{\mathbf{q}}(b^{\dagger}_{-\mathbf{q}})$,

$$U(\mathbf{r}) = \sum_{\mathbf{q}} \left(\frac{\hbar}{2NM\omega_{\mathbf{q}}} \right)^{1/2} e^{i\mathbf{q}\cdot\mathbf{r}} (b_{\mathbf{q}} + b^{\dagger}_{-\mathbf{q}}), \tag{44}$$

where N denotes the number of unit cells, M is the mass of the Carbon atom, and we assume an isotropic phonon dispersion $\omega_{\mathbf{q}} = v_s q$. To determine the pairing interaction mediated by LA' phonons, we work in the band basis $c^{\dagger}_{\mathbf{k},\alpha} = \sum_{\sigma} u^{\star}_{\alpha\sigma}(\mathbf{k}) c^{\dagger}_{\mathbf{k}\sigma}$, where α denotes the band index, and perform a Schrieffer-Wolff transformation (with $\eta = D(\hbar L^2/(2NM\omega_q))^{1/2}$) on the band-projected electron-phonon interaction. The effective pairing Hamiltonian H_{pair} for the BCS pair $(\mathbf{k} + \mathbf{Q}; -\mathbf{k} + \mathbf{Q})$ with a center of mass momentum $2\mathbf{Q}$, takes the form

$$H_{pair} = \frac{1}{L^2} \sum_{\mathbf{k},\mathbf{k}',\mathbf{Q}} V_{\mathbf{k},\mathbf{k}',\mathbf{Q}} c^{\dagger}_{\mathbf{k}+\mathbf{Q}} c^{\dagger}_{-\mathbf{k}+\mathbf{Q}} c_{-\mathbf{k}'+\mathbf{Q}} c_{\mathbf{k}'+\mathbf{Q}}, \tag{45}$$

with an effective interaction

$$V_{\mathbf{k},\mathbf{k}',\mathbf{Q}} = -A_{uc} \left(\frac{D}{\hbar v_s} \right)^2 \frac{\hbar^2}{2M} \Gamma_{\mathbf{k},\mathbf{k}',\mathbf{Q}} = -G_0 \Gamma_{\mathbf{k},\mathbf{k}',\mathbf{Q}}, \tag{46}$$

where A_{uc} is the area of the unit cell, and we neglect the retardation effect of the pairing interaction, and

$$\Gamma_{\mathbf{k},\mathbf{k}',\mathbf{Q}} = \langle u_{\alpha,\mathbf{k}+\mathbf{Q}} | u_{\alpha,\mathbf{k}'+\mathbf{Q}} \rangle \langle u_{\alpha,-\mathbf{k}+\mathbf{Q}} | u_{\alpha,-\mathbf{k}'+\mathbf{Q}} \rangle, \tag{47}$$

encodes the effect of band geometry on the effective pairing interaction. Notice that with the assumption of a linear phonon dispersion, the magnitude of the effective interaction becomes Qq-independent.

Estimates of the electron-phonon pairing attraction

In this subsection, we calculate the effective pairing attraction due to LA' and LO' phonons in rhombohedral graphene. Our estimates indicate that longitudinal acoustic (LA') phonons provide the leading contribution to the effective pairing interaction for a circular Fermi surface. Neglecting the retardation effects (i.e., assuming frequency-independent pairing), the effective pairing interaction G_0 due to the LA' phonons can be estimated as

$$G_0 = D\Big(\frac{\hbar A_{u.c}}{2Mv_s}\Big)\frac{1}{\hbar v_s} = \frac{\sqrt{3}}{2}a_0^2\Big(\frac{D}{\hbar v_s}\Big)^2\frac{\hbar}{2M}, \tag{48}$$

where M denotes the mass of the Carbon atom, $A_{u.c} = \sqrt{3}/2a_0^2$ is the unit cell area, v_s is the phonon sound velocity. Since the other parameters are known, we express this value in terms of $D/(\hbar v_s)$, giving

$$g_{ac} = \frac{\sqrt{3}}{2}(0.246)^2\frac{(197.3)^2}{2\times 12\times 1836\times 511000}\Big(\frac{D}{\hbar v_s}\Big)^2 = 9.24\times 10^{-8}\Big(\frac{D}{\hbar v_s}\Big)^2. \tag{49}$$

For LA phonon in graphene we used $v_s = 2\times 10^4$ m/s and $D = 15$ eV, leading to $\hbar v_s = 0.013$ eV nm, which gives

$$g_{ac} = 9.24\times 10^{-8}\Big(\frac{15}{0.013}\Big)^2 = 123\text{meV.nm}^2. \tag{50}$$

We note that Ref. [1] uses $D = 30$ eV for the deformation field giving $G_0 = 482\text{meV.nm}^2$. Following along the same lines, we can define an effective coupling for the optical phonons. In this case, the effective pairing attraction due to the optical phonons is given by [3]

$$G_{op} = F\Big(\frac{\hbar A_{u.c}}{2M\omega}\Big)\frac{1}{\hbar\omega} = \frac{\sqrt{3}}{2}a_0^2\Big(\frac{F}{\hbar\omega}\Big)^2\frac{\hbar}{2M}, \tag{51}$$

where F denotes the electron-phonon coupling, and $\hbar\omega$ is the optical frequency. This gives

$$G_{op} = \frac{\sqrt{3}}{2}(0.246)^2\frac{(197.3)^2}{2\times 12\times 1836\times 511000}\Big(\frac{F}{\hbar\omega}\Big)^2 = 9.24\times 10^{-8}\Big(\frac{F}{\hbar\omega}\Big)^2. \tag{52}$$

For the optical phonon in graphene, Ref. [3] estimated this coupling from the tight-binding model as

$$F = 3\beta\sqrt{\frac{3}{2}}\Big(\frac{t_0}{a_0}\Big) = 3\times 3.3\times\sqrt{\frac{3}{2}}\Big(\frac{3}{0.246}\Big) = 147.86. \tag{53}$$

The optical phonon energies associated with the E_1 and A_1 are 0.196 eV and 0.17 eV respectively, giving an effective pairing attraction,

$$G_{E_2} = 9.24\times 10^{-8}\Big(\frac{147.86}{0.17}\Big)^2 = 69\text{meV.nm}^2, \qquad G_{A_1} = 9.24\times 10^{-8}\Big(\frac{147.86}{0.196}\Big)^2 = 51\text{meV.nm}^2, \tag{54}$$

which is smaller than the LA' phonon mediated pairing attraction. We don't anticipate this LO' phonon-mediated attraction to change significantly for rhombohedral graphene. Our estimates indicate that optical phonon–mediated pairing, proposed as a possible mechanism in twisted bilayer graphene [3–5], is weaker than the LA' phonon–mediated interaction. The estimated strength of the LO' induced pairing interaction is approximately ~ 70 meV nm^2 [3], about half that of the LA' phonon–mediated counterpart.

PAIRING INTERACTION IN THE TWO-VALLEY MODEL

The Fermi surfaces consist of two electron-like or hole-like valleys below (above) half-filling of the valence (conduction) bands at each valley. We treat the Fermi surfaces as circular in the following analysis. The Fermi surfaces are separated by the $\mathbf{Q} = (4\pi/3, 0)$. In the two-valley model, the interactions can be divided into four types denoted below by $G_1(\mathbf{p}, \mathbf{p}'), G_2(\mathbf{p}, \mathbf{p}'), G_3(\mathbf{p}, \mathbf{p}')$, and $G_4(\mathbf{p}, \mathbf{p}')$ using the usual representation of the pairing interactions in the literature. In rhombohedral graphene, one Fermi surface resides at the $\mathbf{K}_D$ point while the other at the $-\mathbf{K}_D$ point. Defining the electron operators near the Fermi surface positioned at the two valleys as $a^\dagger_{\mathbf{p}} = c^\dagger_{\mathbf{p}+\mathbf{K}_D}$ and $b^\dagger_{\mathbf{p}} = c^\dagger_{\mathbf{p}-\mathbf{K}_D}$, we can express the pairing interaction as

$$H_{int} = \frac{1}{L^2}\sum_{\mathbf{p},\mathbf{p}'}\Big[G_1(\mathbf{p},\mathbf{p}')a^\dagger_{\mathbf{p}}b^\dagger_{-\mathbf{p}}b_{-\mathbf{p}'}a_{\mathbf{p}'} + G_2(\mathbf{p},\mathbf{p}')a^\dagger_{\mathbf{p}}b^\dagger_{-\mathbf{p}}a_{-\mathbf{p}'}b_{-\mathbf{p}'} + G_3(\mathbf{p},\mathbf{p}')[a^\dagger_{\mathbf{p}}a^\dagger_{-\mathbf{p}}b_{-\mathbf{p}'}b_{\mathbf{p}'} + b^\dagger_{\mathbf{p}}b^\dagger_{-\mathbf{p}}a_{-\mathbf{p}'}a_{\mathbf{p}'}]$$
$$+ G_4(\mathbf{p},\mathbf{p}')[a^\dagger_{\mathbf{p}}a^\dagger_{-\mathbf{p}}a_{-\mathbf{p}'}a_{\mathbf{p}'} + b^\dagger_{\mathbf{p}}b^\dagger_{-\mathbf{p}}b_{-\mathbf{p}'}b_{\mathbf{p}'}]\Big]. \tag{55}$$

Each of these terms corresponds to a physically distinct interaction. The interaction matrix elements G_1 and G_2 correspond to inter-valley scattering and inter-valley exchange interactions, respectively. The intra-valley interactions G_4 and G_3 correspond to intra-valley pairing and the Cooper pair tunneling process. The pairing interactions (G_1, G_2) lead to inter-valley pairing $\langle a^\dagger_{\mathbf{p}}b^\dagger_{-\mathbf{p}}\rangle \neq 0$, while the pairing interactions (G_3, G_4) lead to intra-valley pairing $\langle a^\dagger_{\mathbf{p}}a^\dagger_{-\mathbf{p}}\rangle \neq 0$ and $\langle b^\dagger_{\mathbf{p}}b^\dagger_{-\mathbf{p}}\rangle \neq 0$. Below, discuss each term and calculate the projected interactions associated with each pairing interaction.

Intervalley Pairing Interaction

- G_1 denotes the inter-valley interaction of electrons in one valley with the electrons in the other valley. This interaction corresponds to four-fermion operator $a^\dagger_{\mathbf{p}}b^\dagger_{-\mathbf{p}}b_{-\mathbf{p}'}a_{\mathbf{p}'}$. The projected pairing interaction for $\mathbf{Q} = 0$ with the pairs $\mathbf{k} = \mathbf{p} + \mathbf{K}_D; \mathbf{k}' = \mathbf{p}' + \mathbf{K}_D$ or the pairs $\mathbf{k} = \mathbf{p} - \mathbf{K}_D; \mathbf{k}' = \mathbf{p}' - \mathbf{K}_D$, gives,

$$G_1(\mathbf{p},\mathbf{p}') = -2G_0\Big[\langle u_{\mathbf{K}_D}(\mathbf{p})|u_{\mathbf{K}_D}(\mathbf{p}')\rangle\langle u_{-\mathbf{K}_D}(-\mathbf{p})|u_{-\mathbf{K}_D}(-\mathbf{p}')\rangle\Big], \tag{56}$$

with G_0 being the strength of the pairing interaction. The factor of 2 results from the other interaction that comes from $\mathbf{p} \leftrightarrow \mathbf{p}'$, which simply interchanges the valleys. This term corresponds to the four-body interaction $b^\dagger_{\mathbf{p}}a^\dagger_{-\mathbf{p}}a_{-\mathbf{p}'}b_{\mathbf{p}'}$. Due to inversion symmetry $\sigma_x H(\mathbf{k})\sigma_x = H(-\mathbf{k})$, giving $|u_{\alpha,-\mathbf{K}_D}(-\mathbf{p})\rangle = \hat{\sigma}_x|u_{\alpha,\mathbf{K}_D}(\mathbf{p})\rangle$. Therefore

$$G_1(\mathbf{p},\mathbf{p}') = -2G_0\Big[\langle u_{\mathbf{K}_D}(\mathbf{p})|u_{\mathbf{K}_D}(\mathbf{p}')\rangle\langle u_{\mathbf{K}_D}(\mathbf{p})|u_{\mathbf{K}_D}(\mathbf{p}')\rangle\Big], \tag{57}$$

Specifically, the $\alpha = +$ wavefunction for the $\mathbf{K}_D$ and $-\mathbf{K}_D$ valley can be expressed as

$$|u_{+,\mathbf{K}_D}(\mathbf{p})\rangle = \begin{pmatrix} u_{\mathbf{p}}e^{-\imath J\varphi_{\mathbf{p}}/2} \\ v_{\mathbf{p}}e^{\imath J\varphi_{\mathbf{p}}/2}\end{pmatrix}, \qquad |u_{+,-\mathbf{K}_D}(-\mathbf{p})\rangle = \begin{pmatrix} v_{\mathbf{p}}e^{\imath J\varphi_{\mathbf{p}}/2} \\ u_{\mathbf{p}}e^{-\imath J\varphi_{\mathbf{p}}/2}\end{pmatrix}, \tag{58}$$

where

$$u_{\mathbf{p}} = \frac{1}{\sqrt{2}}\Big(1 + \frac{m}{\sqrt{\zeta_J p^{2J} + m^2}}\Big)^{1/2}, \qquad v_{\mathbf{p}} = \frac{1}{\sqrt{2}}\Big(1 - \frac{m}{\sqrt{\zeta_J p^{2J} + m^2}}\Big)^{1/2}. \tag{59}$$

With this gauge choice, the evaluation for the chiral model gives, near the Fermi surface, $p_x = p_F\cos(\varphi_{\mathbf{p}})$, $p_y = p_F\sin(\varphi_{\mathbf{p}})$ and $|\mathbf{p}| \sim |\mathbf{p}'| \sim p_F$,

$$G_1(\mathbf{p},\mathbf{p}') = -2G_0\frac{e^{-\imath J(\varphi_{\mathbf{p}}+\varphi_{\mathbf{p}'})}}{4(\xi_p+\mu)^2}\Big(e^{\imath J\varphi_{\mathbf{p}'}}(\xi_p+\mu-m) + e^{\imath J\varphi_{\mathbf{p}}}(\xi_p+\mu+m)\Big)^2 \tag{60}$$
$$= -G_0\Big(1 - \frac{m^2}{(\xi_p+\mu)^2}\Big) - e^{-\imath J\phi}\frac{G_0}{2}\Big(1 - \frac{m}{\xi_p+\mu}\Big)^2 - e^{\imath J\phi}\frac{G_0}{2}\Big(1 + \frac{m}{\xi_p+\mu}\Big)^2, \tag{61}$$

where $\phi = \varphi_{\mathbf{p}} - \varphi_{\mathbf{p}'}$ defines the relative momentum on the circular Fermi surface.

- G_2 denotes the exchange of electrons in one valley with the electrons in the other valley. This interaction corresponds to four-fermion operator $a^\dagger_{\mathbf{p}} b^\dagger_{-\mathbf{p}} a_{-\mathbf{p}'} b_{\mathbf{p}'}$. This term corresponds to the four-body interaction $b^\dagger_{\mathbf{p}} a^\dagger_{-\mathbf{p}} b_{-\mathbf{p}'} a_{\mathbf{p}'}$. The projected pairing interaction for $\mathbf{Q} = 0$ with the pairs $\mathbf{k} = \mathbf{p} + \mathbf{K}_D; \mathbf{k}' = \mathbf{p}' - \mathbf{K}_D$ or $\mathbf{k} = \mathbf{p} - \mathbf{K}_D; \mathbf{k}' = \mathbf{p}' + \mathbf{K}_D$, gives

$$G_2(\mathbf{p}, \mathbf{p}') = -2G_0 \Big[\langle u_{\mathbf{K}_D}(\mathbf{p}) | u_{-\mathbf{K}_D}(\mathbf{p}') \rangle \langle u_{-\mathbf{K}_D}(-\mathbf{p}) | u_{\mathbf{K}_D}(-\mathbf{p}') \rangle \Big]. \tag{62}$$

Again, the factor of 2 comes from the other interaction from $\mathbf{p} \leftrightarrow \mathbf{p}'$, which simply interchanges the valleys. Using inversion symmetry, we can write

$$|u_{-\mathbf{K}_D}(\mathbf{p}')\rangle = \sigma_x |u_{\mathbf{K}_D}(-\mathbf{p}')\rangle, \tag{63}$$

which implies

$$G_2(\mathbf{p}, \mathbf{p}') = -2G_0 \Big[\langle u_{\mathbf{K}_D}(\mathbf{p}) | u_{-\mathbf{K}_D}(\mathbf{p}') \rangle \langle u_{\mathbf{K}_D}(\mathbf{p}) | u_{-\mathbf{K}_D}(\mathbf{p}') \rangle \Big]. \tag{64}$$

The wavefunction for $|u_{-\mathbf{K}_D}(\mathbf{p}')\rangle$, can be attained from $\mathbf{p}' \to -\mathbf{p}'$ and $\varphi_{-\mathbf{p}'} \to \varphi_{\mathbf{p}'} + \pi$, giving

$$|u_{-\mathbf{K}_D}(\mathbf{p}')\rangle = \begin{pmatrix} e^{\imath J\pi/2} v_{\mathbf{p}} e^{\imath J \varphi_{\mathbf{p}}/2} \\ e^{-\imath J\pi/2} u_{\mathbf{p}} e^{-\imath J \varphi_{\mathbf{p}}/2} \end{pmatrix}. \tag{65}$$

Evaluation of the interaction matrix elements of the chiral model gives, near the Fermi surface $p_x = p_F \cos(\varphi_{\mathbf{p}}), p_y = p_F \sin(\varphi_{\mathbf{p}})$ and $|\mathbf{p}| \sim |\mathbf{p}'| \sim p_F$, gives.

$$G_2(\mathbf{p}, \mathbf{p}') = -G_0 \Big[1 + (-1)^J \cos(J\Phi) \Big] \Big(1 - \frac{m^2}{(\xi_p + \mu)^2} \Big), \tag{66}$$

making the interaction dependent on the even or odd value of the chirality J, where $\Phi = \varphi_{\mathbf{p}} + \varphi_{\mathbf{p}'}$.

Intravalley Pairing Interaction

- G_4 denotes the intra-valley interaction of electrons within the same valley. Due to inversion symmetry the pair interaction corresponding $a^\dagger_{\mathbf{p}} a^\dagger_{-\mathbf{p}} a_{-\mathbf{p}'} a_{\mathbf{p}'}$ is equal to the pair interaction for the other valley $b^\dagger_{\mathbf{p}} b^\dagger_{-\mathbf{p}} b_{-\mathbf{p}'} b_{\mathbf{p}'}$. The $a^\dagger_{\mathbf{p}} a^\dagger_{-\mathbf{p}} a_{-\mathbf{p}'} a_{\mathbf{p}'}$ interaction matrix element is given by,

$$G_4(\mathbf{p}, \mathbf{p}') = -G_0 \Big[\langle u_{\mathbf{K}_D}(\mathbf{p}) | u_{\mathbf{K}_D}(\mathbf{p}') \rangle \langle u_{\mathbf{K}_D}(\mathbf{p}) | u_{\mathbf{K}_D}(\mathbf{p}') \rangle \Big], \tag{67}$$

while the $b^\dagger_{\mathbf{p}} b^\dagger_{-\mathbf{p}} b_{-\mathbf{p}'} b_{\mathbf{p}'}$ interaction matrix element is given by,

$$G_4(\mathbf{p}, \mathbf{p}') = -G_0 \Big[\langle u_{-\mathbf{K}_D}(-\mathbf{p}) | u_{-\mathbf{K}_D}(-\mathbf{p}') \rangle \langle u_{-\mathbf{K}_D}(-\mathbf{p}) | u_{-\mathbf{K}_D}(-\mathbf{p}') \rangle \Big], \tag{68}$$

$$= -G_0 \Big[\langle u_{\mathbf{K}_D}(\mathbf{p}) | u_{\mathbf{K}_D}(\mathbf{p}') \rangle \langle u_{\mathbf{K}_D}(\mathbf{p}) | u_{\mathbf{K}_D}(\mathbf{p}') \rangle \Big]. \tag{69}$$

Again evaluation near the Fermi surface $p_x = p_F \cos(\varphi_{\mathbf{p}}), p_y = p_F \sin(\varphi_{\mathbf{p}})$ and $|\mathbf{p}| \sim |\mathbf{p}'| \sim p_F$, gives

$$G_4(\mathbf{p}, \mathbf{p}') = -G_0 \frac{e^{-\imath J(\varphi_{\mathbf{p}} + \varphi_{\mathbf{p}'})}}{4(\xi_p + \mu)^2} \Big(e^{\imath J \varphi_{\mathbf{p}'}} (\xi_p + \mu - m) + e^{\imath J \varphi_{\mathbf{p}}} (\xi_p + \mu + m) \Big)^2 \tag{70}$$

$$= -\frac{G_0}{2} \Big(1 - \frac{m^2}{(\xi_p + \mu)^2} \Big) - G_0 \frac{e^{-\imath J\phi}}{4} \Big(1 - \frac{m}{\xi_p + \mu} \Big)^2 - G_0 \frac{e^{\imath J\phi}}{4} \Big(1 + \frac{m}{\xi_p + \mu} \Big)^2, \tag{71}$$

which equals the $2G_1$ interaction due to inversion symmetry. Note that this is only true for orbital-independent interactions.

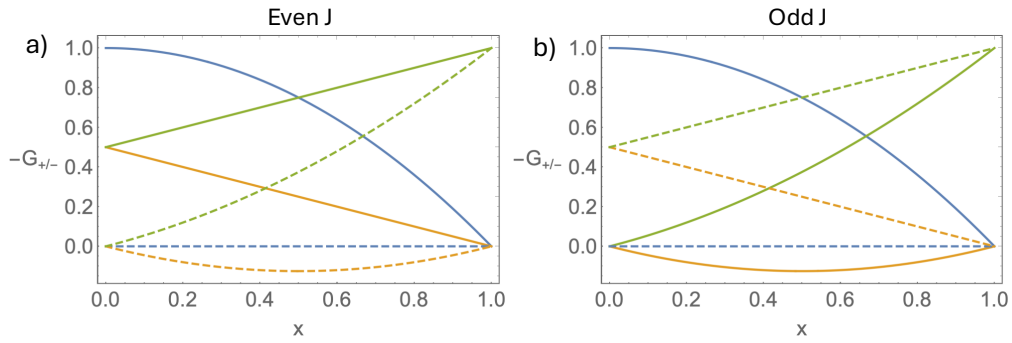


FIG. 3: Angular momentum decomposition for the interaction matrix elements $G_{\pm,l}$ for the chiral model with (a) even chirality and (b) odd chirality. The solid (dotted) lines denote $G_{+,l}(G_{-,l})$ with $(l = 0)$ blue curve, $(l = J)$ orange curve and $(l = -J)$ green curve as a function of $x = m/\mu$.

- G_3 denotes the Cooper pair tunneling of from one valley $a^\dagger_{\mathbf{p}}(b^\dagger_{\mathbf{p}})$ to the other valley $b^\dagger_{\mathbf{p}}(a^\dagger_{\mathbf{p}})$. The projected pairing interaction for the $a^\dagger_{\mathbf{p}}a^\dagger_{-\mathbf{p}}b_{-\mathbf{p}'}b_{\mathbf{p}'}$ and the $b^\dagger_{\mathbf{p}}b^\dagger_{-\mathbf{p}}a_{-\mathbf{p}'}a_{\mathbf{p}'}$, which is equal due to inversion symmetry, is given by

$$G_3(\mathbf{p},\mathbf{p}') = -G_0\Big[\langle u_{\mathbf{K}_D}(\mathbf{p})|u_{-\mathbf{K}_D}(\mathbf{p}')\rangle\langle u_{\mathbf{K}_D}(\mathbf{p})|u_{-\mathbf{K}_D}(\mathbf{p}')\rangle\Big]. \tag{72}$$

Evaluation for the chiral model gives near the Fermi surface $p_x = p_F\cos(\varphi_{\mathbf{p}})$, $p_y = p_F\sin(\varphi_{\mathbf{p}})$ and $|\mathbf{p}| \sim |\mathbf{p}'| \sim p_F$, gives.

$$G_3(\mathbf{p},\mathbf{p}') = -G_0\Big[\cos\Big(\frac{J(\varphi_{\mathbf{p}}+\varphi_{\mathbf{p}'})}{2}\Big)\Big]^2\Big(1-\frac{m^2}{(\xi_p+\mu)^2}\Big) = -\frac{G_0}{2}\Big[1+(-1)^J\cos(J\Phi)\Big]\Big(1-\frac{m^2}{(\xi_p+\mu)^2}\Big). \tag{73}$$

From the expression of the pairing interactions, it is clear that we have the relations that $G_1(\mathbf{p},\mathbf{p}') = 2G_4(\mathbf{p},\mathbf{p}')$ and $G_2(\mathbf{p},\mathbf{p}') = 2G_3(\mathbf{p},\mathbf{p}')$. To summarize, we get

$$G_4(\mathbf{p},\mathbf{p}') = -\frac{G_0}{2}\Big(1-\frac{m^2}{(\xi_p+\mu)^2}\Big) - \frac{G_0e^{-\imath J\phi}}{4}\Big(1-\frac{m}{\xi_p+\mu}\Big)^2 - \frac{G_0e^{\imath J\phi}}{4}\Big(1+\frac{m}{\xi_p+\mu}\Big)^2, \tag{74}$$

$$G_3(\mathbf{p},\mathbf{p}') = -\frac{G_0}{2}\Big(1-\frac{m^2}{(\xi_p+\mu)^2}\Big) + \frac{(-1)^JG_0e^{\imath J\Phi}}{4}\Big(1-\frac{m^2}{(\xi_p+\mu)^2}\Big) + \frac{(-1)^JG_0e^{-\imath J\Phi}}{4}\Big(1-\frac{m^2}{(\xi_p+\mu)^2}\Big). \tag{75}$$

Decompsition into angular momentum channels (J = even)

To decompose any interaction in the angular momentum channel, we express the general interaction matrix elements $G_i(\mathbf{p},\mathbf{p}')$ in terms of relative angular momentum on the Fermi surface. We assume a ciruclar Fermi surface and write $G_i(p_F,p_F,\phi)$ where p_F is the Fermi wavevector and $\phi = \varphi_{\mathbf{p}} - \varphi_{\mathbf{q}}$ is the relative angle. We can perform the decomposition of the interaction matrix elements asscoiated with $G_1(\mathbf{p},\mathbf{p}')$ and $G_4(\mathbf{p},\mathbf{p}')$ simply by inspection, taking $\varphi_{\mathbf{p}} = 0$, i.e. taking $\mathbf{p}$ along the $\hat{k}_x-$ direction. There are only three components for the minimal chiral model $l = 0, J, -J$, and for $|\mathbf{p}| = |\mathbf{p}'| \sim p_F$, with $\xi_{p_F} = 0$, one arrives as

$$G_{4,0} = -\frac{G_0}{2}(1-x^2), \qquad G_{4,J} = -\frac{G_0}{4}(1-x)^2, \qquad G_{4,-J} = -\frac{G_0}{4}(1+x)^2. \tag{76}$$

Similarly for the Cooper pair tunnelling $G_3(\mathbf{p},\mathbf{p}')$ we have,

$$G_{3,0} = -\frac{G_0}{2}(1-x^2), \qquad G_{3,J} = -\frac{G_0}{4}(1-x^2), \qquad G_{3,-J} = -\frac{G_0}{4}(1-x^2). \tag{77}$$

Since time-reversal symmetry is broken, we find that $G_{4,J} \neq G_{4,-J}$. In addition, $G_{4,J} > G_{4,0}$, so the chiral-J pairing dominates in this channel. However, as we see in the next section, we must include the Cooper pair tunneling to understand the pairing interaction and calculate $G_+ = G_4 + G_3$ in each channel, which gives

$$G_{+,0} = -G_0(1-x^2), \qquad G_{+,J} = -\frac{G_0}{2}(1-x), \qquad G_{+,-J} = -\frac{G_0}{2}(1+x), \tag{78}$$

and for $G_- = G_4 - G_3$

$$G_{-,0} = 0, \qquad G_{-,J} = -\frac{G_0}{2}x(x-1), \qquad G_{-,-J} = -\frac{G_0}{2}x(x+1). \tag{79}$$

Decompsition into angular momentum channels (J = odd)

Again we can perform the decomposition of the interaction matrix elements associated with $G_1(\mathbf{p},\mathbf{p}')$ and $G_4(\mathbf{p},\mathbf{p}')$ simply by inspection, taking $\varphi_{\mathbf{p}} = 0$, i.e. taking $\mathbf{p}$ along the $\hat{k}_x-$ direction. The angular momentum decomposition of $G_4(\mathbf{p},\mathbf{p}')$ is the same as above.

$$G_{4,0} = -\frac{G_0}{2}(1-x^2), \qquad G_{4,J} = -\frac{G_0}{4}(1-x)^2, \qquad G_{4,-J} = -\frac{G_0}{4}(1+x)^2. \tag{80}$$

However, since $G_3(\mathbf{p},\mathbf{p}')$ depends on the parity of the chiral index, we find a repulsive interaction in the chiral channel $J, -J$.

$$G_{3,0} = -\frac{G_0}{2}(1-x^2), \qquad G_{3,J} = \frac{G_0}{4}(1-x^2), \qquad G_{3,-J} = \frac{G_0}{4}(1-x^2). \tag{81}$$

Calculation of $G_+ = G_4 + G_3$ in each channel which gives

$$G_{+,0} = -G_0(1-x^2), \qquad G_{+,J} = -\frac{G_0}{2}x(1-x), \qquad G_{+,-J} = -\frac{G_0}{2}x(x+1), \tag{82}$$

and for $G_- = G_4 - G_3$

$$G_{-,0} = 0, \qquad G_{-,J} = -\frac{G_0}{2}(1-x), \qquad G_{-,-J} = -\frac{G_0}{2}(1+x). \tag{83}$$

Fig. 3 (a) and (b) show the angular momentum decomposition for the interaction matrix elements $G_{\pm,l}$ for the chiral model for even chirality (a) and odd chirality (b).

RENORMALIZATION GROUPS ANALYSIS OF KEKULÉ SUPERCONDUCTIVITY IN CHIRAL 2DEGS

Superconducting instability for a single Fermi surface

First, consider a time-reversal- and inversion-symmetric Fermi surface. We know that such a Fermi surface has a pairing instability, due to the presence of a logarithmic divergence in the pair susceptibility at Π at $\mathbf{q} = 0$, given by

$$\Pi(\mathbf{q}=0) = \frac{1}{\beta}\sum_{i\omega}\int \frac{d^2\mathbf{k}}{(2\pi)^2} G(\mathbf{k}, i\omega)G(-\mathbf{k}, -i\omega) = N(0)\log\left(\frac{E_c}{T}\right), \tag{84}$$

where $G(\mathbf{k}, i\omega)$ denotes the single particle Green's function, $N(0)$ denotes the density of states at the Fermi level, E_0 is the bandwidth or Debye frequency cutoff, $\beta = k_B T$, and for simplicity we take $k_B = 1$. We consider interactions at $\mathbf{q} = 0$ center of mass momentum between the pairs $(\mathbf{k}, \uparrow; -\mathbf{k}, \downarrow)$,

$$H = \frac{1}{L^2}\sum_{\mathbf{k},\mathbf{k}'} V_{\mathbf{k},\mathbf{k}'} c^\dagger_{\mathbf{k},\uparrow} c^\dagger_{-\mathbf{k},\downarrow} c_{-\mathbf{k}',\downarrow} c_{\mathbf{k}',\uparrow}. \tag{85}$$

The renormalized interaction to second order in the interaction strength in the Cooper channel can be expressed in terms of the Feynman diagram in Fig 4. We would like to point out that other non-sigular particle-hole diagrams for a circular Fermi surface have been ignored. These diagrams can't be neglected in the vicinity of van Hove singularities. Using Feynman rules, we get the second-order renormalized interaction vertex $V^r_{\mathbf{k},\mathbf{k}'}$

$$-V^r_{\mathbf{k},\mathbf{k}'} = (-V_{\mathbf{k},\mathbf{k}'}) + \frac{1}{\beta}\sum_{i\omega_1}\int \frac{d^2\mathbf{k}_1}{(2\pi)^2} V_{\mathbf{k},\mathbf{k}_1} V_{\mathbf{k}_1,\mathbf{k}'} G(\mathbf{k}_1, i\omega_1)G(-\mathbf{k}_1, -i\omega_1). \tag{86}$$

To proceed, we decompose the interaction in the irreducible representations near the Fermi surface $|\mathbf{k}| \simeq |\mathbf{k}'| \simeq k_F$, giving

$$V_{\mathbf{k},\mathbf{k}'} = \sum_l V_l \Gamma_l(\hat{\mathbf{k}})\Gamma_l(\hat{\mathbf{k}}'), \tag{87}$$

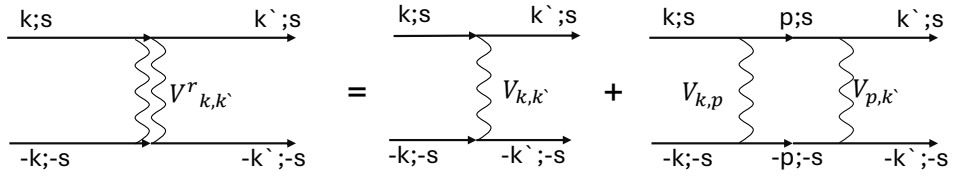


FIG. 4: Feynman diagrams for the renormalization of the interaction vertex of a single Fermi surface, due to interactions in the BCS channel.

where l labels the pairing channel. Plugging the interaction gives

$$\sum_l V_l^r \Gamma_l(\hat{\mathbf{k}})\Gamma_l(\hat{\mathbf{k}'}) = \sum_l V_l \Gamma_l(\hat{\mathbf{k}})\Gamma_l(\hat{\mathbf{k}'}) - \sum_{l,l'}(V_l)(V_{l'})\Gamma_l(\hat{\mathbf{k}})\Gamma_{l'}(\hat{\mathbf{k}'})\frac{1}{\beta}\sum_{i\omega_1}\int \frac{d^2\mathbf{k}_1}{(2\pi)^2}\Gamma_l(\hat{\mathbf{k}_1})\Gamma_{l'}(\hat{\mathbf{k}_1})G(\mathbf{k}_1, i\omega_1)G(-\mathbf{k}_1, -i\omega_1). \quad (88)$$

which, due to the orthogonality of different irreps

$$\int d\hat{\mathbf{k}_1}\Gamma_l(\hat{\mathbf{k}_1})\Gamma_{l'}(\hat{\mathbf{k}_1}) = \delta_{l,l'}, \quad (89)$$

gives

$$V_l^r = V_l - V_l^2\frac{1}{\beta}\sum_{i\omega_1}\int \frac{d^2\mathbf{k}_1}{(2\pi)^2}G(\mathbf{k}_1, i\omega_1)G(-\mathbf{k}_1, -i\omega_1) \quad (90)$$

$$V_l^r = V_l - V_l^2 N(0)\log\left(\frac{E_c}{T}\right). \quad (91)$$

This indicates that the renormalized interactions in different irreps are independent of one another.

Defining $y_l = N(0)V_l$ and $t = \log(E_0/T)$ we can write this as a differential equation for the y_l

$$\frac{dy_l}{dt} = -y_l^2, \quad (92)$$

which can be solved easily

$$\int_{y_l(0)}^{y_l(t)}\frac{dy}{y_l^2} = -\int_0^t dt \qquad \Longrightarrow \qquad \frac{1}{y_l(0)} - \frac{1}{y_l(t)} = -t, \quad (93)$$

giving the solution

$$y_l(t) = \frac{y_l(0)}{1 + y_l(0)t}. \quad (94)$$

The RG equation for the renormalized interaction is

$$V_l^r(t) = \frac{V_l}{1 + V_l N(0)\log(E_0/T)}. \quad (95)$$

which corresponds to a pole for attractive interactions $V_l = -|V_l|$ giving the critical temperature T_c

$$1 - |V_l|N(0)\log(E_0/T_c) = 0, \qquad \Longrightarrow \qquad T_c = E_0\exp\left(\frac{-1}{N(0)|V_l|}\right). \quad (96)$$

Superconducting instability in chiral 2DEGs

Now, let's look at the case of two Fermi surfaces at different valleys. Defining the electron operators near the Fermi surface positioned at the $\mathbf{K}_D(-\mathbf{K}_D)$ as $a_{\mathbf{p}}^\dagger = c_{\mathbf{p}+\mathbf{K}_D}^\dagger$ and $b_{\mathbf{p}}^\dagger = c_{\mathbf{p}-\mathbf{K}_D}^\dagger$, we can express the pairing interaction as

$$H_{pair} = \frac{1}{L^2}\sum_{\mathbf{p},\mathbf{p}'}\Big[G_1(\mathbf{p},\mathbf{p}')a_{\mathbf{p}}^\dagger b_{-\mathbf{p}}^\dagger b_{-\mathbf{p}'}a_{\mathbf{p}'} + G_2(\mathbf{p},\mathbf{p}')a_{\mathbf{p}}^\dagger b_{-\mathbf{p}}^\dagger a_{-\mathbf{p}'}b_{-\mathbf{p}'}$$
$$+ \frac{G_3(\mathbf{p},\mathbf{p}')}{2}[a_{\mathbf{p}}^\dagger a_{-\mathbf{p}}^\dagger b_{-\mathbf{p}'}b_{\mathbf{p}'} + b_{\mathbf{p}}^\dagger b_{-\mathbf{p}}^\dagger a_{-\mathbf{p}'}a_{\mathbf{p}'}] + \frac{G_4(\mathbf{p},\mathbf{p}')}{2}[a_{\mathbf{p}}^\dagger a_{-\mathbf{p}}^\dagger a_{-\mathbf{p}'}a_{\mathbf{p}'} + b_{\mathbf{p}}^\dagger b_{-\mathbf{p}}^\dagger b_{-\mathbf{p}'}b_{\mathbf{p}'}]\Big]. \quad (97)$$

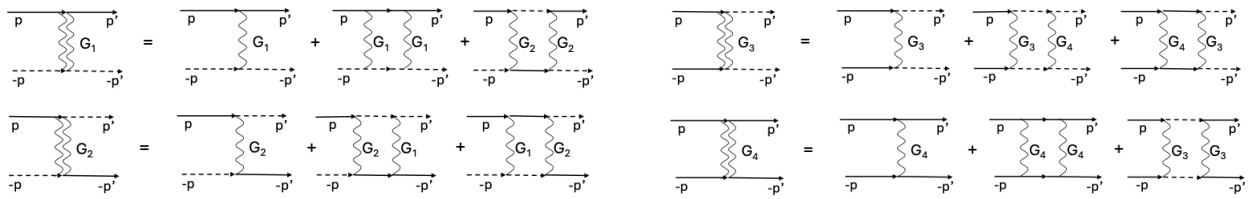


FIG. 5: Feynman diagrams for the renormalization of the interaction vertices G_i for spin polarized chiral 2DEGs.

For the problem we consider, there are two momenta at which the pair susceptibility diverges: $\mathbf{Q} = 0$ and $\mathbf{Q} = \mathbf{K}_D$. We can express the pair susceptibility at these two momenta as

$$\Pi(\mathbf{q} = 0) = \frac{1}{\beta}\sum_{i\omega_1}\int \frac{d^2\mathbf{p}_1}{(2\pi)^2} G_1 G_1 \mathscr{G}(\mathbf{p}_1, i\omega_1)\mathscr{G}(-\mathbf{p}_1, -i\omega_1) = N(0)\log\left(\frac{E_c}{T}\right) f_D(x), \tag{98}$$

$$\Pi(\mathbf{q} = 2\mathbf{K}_D) = \frac{1}{\beta}\sum_{i\omega_1}\int \frac{d^2\mathbf{p}_1}{(2\pi)^2} G_1 G_1 \mathscr{G}(\mathbf{p}_1, i\omega_1)\mathscr{G}(-\mathbf{p}_1 + 2\mathbf{K}_D, -i\omega_1) = N(0)\log\left(\frac{E_c}{T}\right) f_S(x), \tag{99}$$

where x is some parameter that controls the relative strength of $f_D(x)$ and $g(x)$, in our case this is $x = m/\mu$ where μ is the chemical potential. $\Pi(\mathbf{Q} = 0)$ and $\Pi(\mathbf{Q} = \mathbf{K}_D)$ correspond to D- and intra-valley pair susceptibility.

Now, we want to write the renormalization group equations for the interactions G_i's. Again, since there is only the Cooper log, we can just limit ourselves to the renormalization in the Cooper channel. The Feynman diagrams corresponding to the renormalization of the interaction vertex are shown in Fig. 5. We can write down the renormalized interactions for G_1 and G_2 from the Feynman rules

$$G_1^r = G_1 - \frac{1}{\beta}\sum_{i\omega_1}\int \frac{d^2\mathbf{p}_1}{(2\pi)^2} G_1 G_1 \mathscr{G}(\mathbf{p}_1, i\omega_1)\mathscr{G}(-\mathbf{p}_1, -i\omega_1) - \frac{1}{\beta}\sum_{i\omega_1}\int \frac{d^2\mathbf{p}_1}{(2\pi)^2} G_2 G_2 \mathscr{G}(\mathbf{p}_1, i\omega_1)\mathscr{G}(-\mathbf{p}_1, -i\omega_1), \tag{100}$$

$$G_2^r = G_2 - \frac{1}{\beta}\sum_{i\omega_1}\int \frac{d^2\mathbf{p}_1}{(2\pi)^2} G_1 G_2 \mathscr{G}(\mathbf{p}_1, i\omega_1)\mathscr{G}(-\mathbf{p}_1, -i\omega_1) - \frac{1}{\beta}\sum_{i\omega_1}\int \frac{d^2\mathbf{p}_1}{(2\pi)^2} G_1 G_2 \mathscr{G}(\mathbf{p}_1, i\omega_1)\mathscr{G}(-\mathbf{p}_1, -i\omega_1), \tag{101}$$

where the $\mathbf{p}$ and $\mathbf{p}'$ dependence of the interactions G_i is implicit. Using orthogonality, we can decompose the interaction into angular momentum channels denoted by l, giving the renormalized interactions

$$G_{1,l}^r = G_{l,1} - G_{1,l}^2 N(0)\log\left(\frac{E_0}{T}\right) f_D(x) - G_{2,l}^2 N(0)\log\left(\frac{E_0}{T}\right) f_D(x), \tag{102}$$

$$G_{2,l}^r = G_{l,1} - 2G_{1,l}G_{2,l} N(0)\log\left(\frac{E_0}{T}\right) f_D(x). \tag{103}$$

Similarly, the renomormalized interactions for G_3 and G_4 are given by

$$G_4^r = G_4 - \frac{1}{\beta}\sum_{i\omega_1}\int \frac{d^2\mathbf{p}_1}{(2\pi)^2} G_4 G_3 \mathscr{G}(\mathbf{p}_1, i\omega_1)\mathscr{G}(-\mathbf{p}_1 + 2\mathbf{K}_D, -i\omega_1) - \frac{1}{\beta}\sum_{i\omega_1}\int \frac{d^2\mathbf{p}_1}{(2\pi)^2} G_3 G_3 \mathscr{G}(\mathbf{p}_1, i\omega_1)\mathscr{G}(-\mathbf{p}_1 + 2\mathbf{K}_D, -i\omega_1), \tag{104}$$

$$G_3^r = G_3 - \frac{1}{\beta}\sum_{i\omega_1}\int \frac{d^2\mathbf{p}_1}{(2\pi)^2} G_3 G_4 \mathscr{G}(\mathbf{p}_1, i\omega_1)\mathscr{G}(-\mathbf{p}_1 + 2\mathbf{K}_D, -i\omega_1) - \frac{1}{\beta}\sum_{i\omega_1}\int \frac{d^2\mathbf{p}_1}{(2\pi)^2} G_3 G_4 \mathscr{G}(\mathbf{p}_1, i\omega_1)\mathscr{G}(-\mathbf{p}_1 + 2\mathbf{K}_D, -i\omega_1), \tag{105}$$

Again, using orthogonality, we can decompose the interaction into angular momentum channels denoted by l, giving the renormalized interactions

$$G_{4,l}^r = G_{4,l} - G_{4,l}^2 N(0)\log\left(\frac{E_0}{T}\right) f_S(x) - G_{3,l}^2 N(0)\log\left(\frac{E_0}{T}\right) f_S(x), \tag{106}$$

$$G_{3,l}^r = G_{3,1} - 2G_{3,l}G_{4,l} N(0)\log\left(\frac{E_0}{T}\right) f_S(x). \tag{107}$$

Using the notation $g_{i,l} = N(0)G_{i,l}$, and $t = \log(E_0/T)$, we can write the RG flow equations for the interactions giving

$$\dot{g}_{1,l} = -(g_{1,l}^2 + g_{2,l}^2) f_D(x), \tag{108}$$
$$\dot{g}_{2,l} = -2g_{1,l}g_{2,l} f_D(x), \tag{109}$$
$$\dot{g}_{3,l} = -2g_{3,l}g_{4,l} f_S(x), \tag{110}$$
$$\dot{g}_{4,l} = -(g_{4,l}^2 + g_{3,l}^2) f_S(x). \tag{111}$$

We can write $g^D_{\pm,l} = g_{1,l} \pm g_{2,l}$ and $g^D_{\pm,l} = g_{1,l} \pm g_{2,l}$ giving the RG equations

$$\dot{g}^D_{\pm,l} = -(g^D_{\pm,l})^2 f_D(x), \qquad \dot{g}^S_{\pm,l} = -(g^S_{\pm,l})^2 f_S(x). \tag{112}$$

The RG equations for the inter-valley pairing give

$$g^D_{+,l}(t) = \frac{g^D_{+,l}}{1 + g^D_{+,l} t f_D(x)}, \qquad g^D_{-,l}(t) = \frac{g^D_{-,l}}{1 + g^D_{-,l} t f_D(x)}. \tag{113}$$

Again, for attractive interactions, we find a pole, corresponding to the respective critical temperatures

$$T^D_{c,+,l} = E_0 \exp\Big(\frac{-1}{|g^D_{+,l}| f_D(x)}\Big), \qquad T^D_{c,-,l} = E_0 \exp\Big(\frac{-1}{|g^D_{-,l}| f_D(x)}\Big). \tag{114}$$

A similar analysis for the intra-valley pairing gives

$$g^S_{+,l}(t) = \frac{g^S_{+,l}}{1 + g^S_{+,l} t f_S(x)}, \qquad g^S_{-,l}(t) = \frac{g^S_{-,l}}{1 + g^S_{-,l} t f_S(x)}. \tag{115}$$

Again, for attractive interactions, we find a pole, corresponding to the respective critical temperatures

$$T^S_{c,+,l} = E_0 \exp\Big(\frac{-1}{|g^S_{+,l}| f_S(x)}\Big), \qquad T^S_{c,-,l} = E_0 \exp\Big(\frac{-1}{|g^S_{-,l}| f_S(x)}\Big). \tag{116}$$

Superconductivity for even chirality

Due to inversion symmetry in the interaction Hamiltonian H_{pair}, we have $G_1 = 2G_4$ and $G_2 = 2G_3$. Of course, the intra-valley pairing channel has double the set of diagrams, so the factor 2 is canceled, therefore, we have $g^S_{\pm,l} = g^D_{\pm,l}$. For the even chirality, we have

$$G_{+,0} = -G_0(1 - x^2), \qquad G_{+,J} = -\frac{G_0}{2}(1 - x), \qquad G_{+,-J} = -\frac{G_0}{2}(1 + x), \tag{117}$$

and for $G_- = G_4 - G_3$

$$G_{-,0} = 0, \qquad G_{-,J} = -\frac{G_0}{2} x(x - 1), \qquad G_{-,-J} = -\frac{G_0}{2} x(x + 1). \tag{118}$$

Based on the calculation of the pair susceptibility, for even chirality, we get

$$f_S(x) = 1, \qquad f_D(x) = \frac{1 - x^2}{2}, \tag{119}$$

where $x = m/\mu$. Since $f_S(x) > f_D(x)$ for all $x \in (0, 1]$, we conclude that for even chirality, intra-valley pairing dominates. Therefore, the only thing we need to determine is the pairing channel $l = 0, -J, J$ that dominates. From Fig. 3 (a), it is clear that the highest T_c will be determined by either $G_{+,-J}$ or $G_{+,0}$, depending on their relative magnitudes. A plot of the pairing channels indicates that the chiral-J state is preferred for $x_c > 0.5$. This is the solution to the equation

$$|G_{+,-J}| \geq |G_{+,0}|, \quad \Longrightarrow \quad 2x^2 + x - 1 \geq 0, \quad \Longrightarrow \quad x_c \geq 1/2, \tag{120}$$

which is the only positive root. Therefore, for a circular Fermi surface, the intra-valley paired state is a chiral-J Kekule superconductor that has the largest T_c when the Fermi energy is

$$\frac{m}{\sqrt{\xi_J^2 p_F^{2J} + m^2}} \geq \frac{1}{2} \qquad \Longrightarrow \qquad p_F \leq \Big(\frac{\sqrt{3}m}{\xi_J}\Big)^{1/J} \qquad \Longrightarrow \qquad n_e \leq \frac{1}{2\pi}\Big(\frac{\sqrt{3}m}{\xi_J}\Big)^{2/J}, \tag{121}$$

where I have used the circular Fermi surface to express the density $n_e = p_F^2/(2\pi)$. Above this density, the system supports an s-wave Kekulè superconducting state.

Superconductivity for odd chirality

Again, due to inversion symmetry, we only have to calculate $G_{\pm,l}$ for one type of interaction. Calculation of $G_+ = G_{4,1} + G_{3,2}$ in each channel which gives

$$G_{+,0} = -G_0(1-x^2), \qquad G_{+,J} = -\frac{G_0}{2}x(1-x), \qquad G_{+,-J} = -\frac{G_0}{2}x(x+1), \tag{122}$$

and for $G_- = G_{4,1} - G_{3,2}$

$$G_{-,0} = 0, \qquad G_{-,J} = -\frac{G_0}{2}(1-x), \qquad G_{-,-J} = -\frac{G_0}{2}(1+x). \tag{123}$$

Based on the calculation of the pair susceptibility, for even chirality, we get

$$f_S(x) = x^2, \qquad f_D(x) = \frac{1-x^2}{2}, \tag{124}$$

where $x = m/\mu$. Since $f_S(x) > f_D(x)$ for $x > 1/\sqrt{3}$, the situation is more complex for odd chirality. To stay unbiased, we will simply calculate the ratios of the critical temperatures for each channel. Since there are 6 channels, we must compare 12 values of T_c, with 6 for inter-valley pairing and 6 for intra-valley pairing. Fortunately, from Fig. 3, we see that one only needs to worry about $G_{+,0}$ and $G_{-,-J}$ as they dominate for both inter-valley and intra-valley pairing over the other interaction matrix elements, which implies we only have to consider 4 values of critical temperatures.

For intra-valley pairing, we get

$$T^D_{c,+,0} = E_0 \exp\left(\frac{-1}{|g_{+,0}|f_S(x)}\right) = E_0 \exp\left(\frac{-1}{N(0)G_0(1-x^2)x^2}\right), \tag{125}$$

and

$$T^D_{c,-,-J} = E_0 \exp\left(\frac{-1}{|g_{-,-J}|f_S(x)}\right) = E_0 \exp\left(\frac{-1}{N(0)G_0(1+x)x^2}\right), \tag{126}$$

and for inter-valley pairing, we get

$$T^S_{c,+,0} = E_0 \exp\left(\frac{-1}{|g_{+,0}|f_D(x)}\right) = E_0 \exp\left(\frac{-2}{N(0)G_0(1-x^2)^2}\right), \tag{127}$$

and

$$T^S_{c,-,-J} = E_0 \exp\left(\frac{-1}{|g_{-,-J}|f_D(x)}\right) = E_0 \exp\left(\frac{-2}{N(0)G_0(1+x)(1-x^2)}\right). \tag{128}$$

Using a characteristic critical temperature scale

$$T_{c,0} = E_0 \exp\left(\frac{1}{N(0)G_0}\right), \tag{129}$$

we find

$$\frac{T^D_{c,+,0}}{T_{c,0}} = \exp\left(\frac{-1}{(1-x^2)x^2}\right), \qquad \frac{T^D_{c,-,-J}}{T_{c,0}} = \exp\left(\frac{-4}{(1+x)x^2}\right), \tag{130}$$

$$\frac{T^S_{c,+,0}}{T_{c,0}} = \exp\left(\frac{-2}{(1-x^2)^2}\right), \qquad \frac{T^S_{c,-,-J}}{T_{c,0}} = \exp\left(\frac{-4}{(1+x)(1-x^2)}\right). \tag{131}$$

For the expressions, we see that for $x > 1/\sqrt{3}$ the dominant critical temperature is associated with intra-valley pairing in the $(-,-J)$ channel. This corresponds to the intra-valley chiral-J pair with a π-phase between the valleys. For $1/2 < x < 1/\sqrt{3}$, the dominant critical temperature is associated with inter-valley pairing in the $(-,-J)$ channel with a π-phase between the two order parameters, and for $x < 1/2$, we have the simple s-wave superconducting state. The ratios of the different critical temperatures, with respect to the dominant temperature in all three regimes, are plotted in Fig. 6. As before, we can determine the critical densities at which each class of superconducting states is stable.

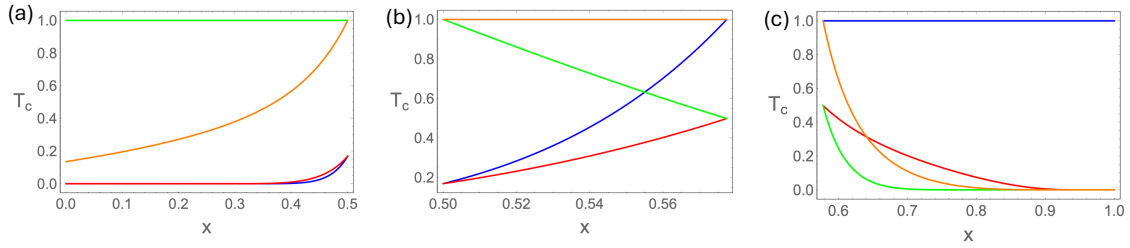


FIG. 6: The ratios of the different critical temperatures, with respect to the dominant temperature in all three regimes: (a) $x > 1/\sqrt{3}$, (b)$1/2 < x < 1/\sqrt{3}$, and (c)$x < 1/2$

The intra-valley paired state is a chiral-J Kekule π-phase superconductor has the largest T_c when $x \geq 1/\sqrt{3}$, or when the Fermi energy is

$$\frac{m}{\sqrt{\xi_J^2 p_F^{2J} + m^2}} \geq \frac{1}{\sqrt{3}}, \qquad \Longrightarrow \qquad p_F \leq \left(\frac{\sqrt{2}m}{\xi_J}\right)^{1/J}, \qquad \Longrightarrow \qquad n_e \leq \frac{1}{2\pi}\left(\frac{\sqrt{2}m}{\xi_J}\right)^{2/J}, \tag{132}$$

where I have used the circular Fermi surface to express the density $n_e = p_F^2/(2\pi)$. When $1/2 \leq x < 1/\sqrt{3}$, we have the inter-valley $\mathbf{Q} = 0$ chiral-J superconducting state with a π-phase between the order parameters, given by

$$\frac{1}{2} \leq \frac{m}{\sqrt{\xi_J^2 p_F^{2J} + m^2}} < \frac{1}{\sqrt{3}}, \quad \Longrightarrow \quad \left(\frac{\sqrt{2}m}{\xi_J}\right)^{1/J} \leq p_F < \left(\frac{\sqrt{3}m}{\xi_J}\right)^{1/J}, \quad \Longrightarrow \quad \frac{1}{2\pi}\left(\frac{\sqrt{2}m}{\xi_J}\right)^{2/J} \leq n_e < \frac{1}{2\pi}\left(\frac{\sqrt{3}m}{\xi_J}\right)^{2/J}. \tag{133}$$

Finally above the density $n_e > 1/(2\pi)(\sqrt{2}m/\xi_J)^{1/J}$ the system supports a conventional s-wave superconductor.

EFFECT OF ELECTRON REPULSION ON THE KEKULÉ SUPERCONDUCTING PHASE

Nearest neighbor repulsion

Within the spin-polarized Haldane phase, the on-site Hubbard U interaction is forbidden, which leaves only the extended Hubbard interactions. In free-standing monolayer graphene, the next-nearest repulsive interaction is estimated to be $U_1 \sim 5.5eV$ based on constrained random phase approximation [6]. Due to the large density of states, we anticipate this value to be smaller in rhombohedral graphene. The interaction strength of the lattice model can be converted to the continuum model by Fourier-transforming to momentum space and then evaluating at the Dirac points. In the spin-polarized case, the nearest-neighbor repulsion can be expressed as

$$H_1 = U_1 \sum_{\mathbf{R},\delta_i} c^\dagger_{\mathbf{R},A} c^\dagger_{\mathbf{R}+\boldsymbol{\delta}_i,B} c_{\mathbf{R}+\boldsymbol{\delta}_i,B} c_{\mathbf{R},A} + c.c., \tag{134}$$

where $\delta_i' s$ denote the three nearest neighbor bonds on the honeycomb lattice $\delta_1 = (0,-1)a_{C-C}$, $\delta_2 = (1, \sqrt{3})a_{C-C}/2$ and $\delta_3 = (-1, \sqrt{3})a_{C-C}/2$, where $a_{C-C} = a_0/\sqrt{3}$ is the Carbon-Carbon distance and $a_0 = 0.241$nm. We ignore the complex conjugate term for now and include it at the end. We introduce the Fourier transform

$$c^\dagger_{\mathbf{R},\sigma} = \frac{1}{\sqrt{N}} \sum_{\mathbf{R}} e^{i\mathbf{k}\cdot\mathbf{R}} c_{\mathbf{k},\sigma}, \tag{135}$$

where N denotes the number of unit cells and $\sigma = A, B$ is the sublattice. The nearest neighbor interaction can then be expressed as

$$H_1 = \frac{U_1}{N} \sum_{\mathbf{k},\mathbf{k}',\mathbf{q}} \mathscr{F}(\mathbf{q}) c^\dagger_{\mathbf{k}+\mathbf{q},A} c^\dagger_{\mathbf{k}'-\mathbf{q},B} c_{\mathbf{k}',B} c_{\mathbf{k},A}, \tag{136}$$

where the lattice form factor $\mathscr{F}(\mathbf{q}) = 1 + e^{i\mathbf{q}\cdot\mathbf{a}_1} + e^{i\mathbf{q}\cdot\mathbf{a}_2}$, with $\mathbf{a}_1 = (1/2, \sqrt{3}/2)a_0$ and $\mathbf{a}_2 = (-1/2, \sqrt{3}/2)a_0$, and $c^\dagger_{\mathbf{k},\sigma}(c_{\mathbf{k},\sigma})$ denote the electron creation (annihilation) operators on the σ sub-lattice. Expressing the interaction in the pair $(\mathbf{k}+\mathbf{Q}; -\mathbf{k}+\mathbf{Q})$ with a

center of mass momentum $2\mathbf{Q}$ and projecting the interaction onto the conduction bands gives

$$H_1 = \frac{1}{L^2}\sum_{\mathbf{k},\mathbf{k}',\mathbf{Q}} U\mathscr{F}(\mathbf{k}-\mathbf{k}')u^{\star}_{A,+}(\mathbf{k}+\mathbf{Q})u^{\star}_{B,+}(-\mathbf{k}+\mathbf{Q})u_{B,+}(-\mathbf{k}'+\mathbf{Q})u_{A,+}(\mathbf{k}'+\mathbf{Q})c^{\dagger}_{\mathbf{k}+\mathbf{Q},+}c^{\dagger}_{-\mathbf{k}+\mathbf{Q},+}c_{-\mathbf{k}'+\mathbf{Q},+}c_{\mathbf{k}'+\mathbf{Q},+}, \tag{137}$$

where $U = U_1 A_{u.c.}$, $A_{u.c.} = \sqrt{3}/2a_0^2$ is the unit cell area with $a_0 = 0.246$ nm, and $c^{\dagger}_{\mathbf{k},+}(c_{\mathbf{k},+})$ denote the conduction band creation (annihilation) operators. The Hamiltonian above contains the four interaction terms corresponding to i) inter-valley scattering, ii) inter-valley exchange interactions, iii) Cooper pair tunneling, and iv) intra-valley pairing. As before, defining the electron operators near the Fermi surface positioned at the $\mathbf{K}_D(-\mathbf{K}_D)$ with $a^{\dagger}_{\mathbf{p}} = c^{\dagger}_{\mathbf{p}+\mathbf{K}_D}$ and $b^{\dagger}_{\mathbf{p}} = c^{\dagger}_{\mathbf{p}-\mathbf{K}_D}$, we can express the repulsive interaction as

$$\begin{aligned} H_1 = \frac{1}{L^2}\sum_{\mathbf{p},\mathbf{p}'}\Big[&U_1(\mathbf{p},\mathbf{p}')a^{\dagger}_{\mathbf{p}}b^{\dagger}_{-\mathbf{p}}b_{-\mathbf{p}'}a_{\mathbf{p}'} + U_2(\mathbf{p},\mathbf{p}')a^{\dagger}_{\mathbf{p}}b^{\dagger}_{-\mathbf{p}}a_{-\mathbf{p}'}b_{-\mathbf{p}'} + U_3(\mathbf{p},\mathbf{p}')[a^{\dagger}_{\mathbf{p}}a^{\dagger}_{-\mathbf{p}}b_{-\mathbf{p}'}b_{\mathbf{p}'} + b^{\dagger}_{\mathbf{p}}b^{\dagger}_{-\mathbf{p}}a_{-\mathbf{p}'}a_{\mathbf{p}'}] \\ &+ U_4(\mathbf{p},\mathbf{p}')[a^{\dagger}_{\mathbf{p}}a^{\dagger}_{-\mathbf{p}}a_{-\mathbf{p}'}a_{\mathbf{p}'} + b^{\dagger}_{\mathbf{p}}b^{\dagger}_{-\mathbf{p}}b_{-\mathbf{p}'}b_{\mathbf{p}'}]\Big]. \end{aligned} \tag{138}$$

where

$$U_1 = 2U\mathscr{F}(\mathbf{p}-\mathbf{p}')u^{\star}_{A,+,\mathbf{K}_D}(\mathbf{p})u^{\star}_{B,+,-\mathbf{K}_D}(-\mathbf{p})u_{B,+,-\mathbf{K}_D}(-\mathbf{p}'),u_{A,+,\mathbf{K}_D}(\mathbf{p}'), \tag{139}$$

$$U_2 = 2U\mathscr{F}(\mathbf{p}-\mathbf{p}'-\mathbf{K}_D)u^{\star}_{A,+,\mathbf{K}_D}(\mathbf{p})u^{\star}_{B,+,-\mathbf{K}_D}(-\mathbf{p})u_{B,+,\mathbf{K}_D}(-\mathbf{p}'),u_{A,+,-\mathbf{K}_D}(\mathbf{p}'), \tag{140}$$

$$U_3 = U\mathscr{F}(\mathbf{p}-\mathbf{p}'+\mathbf{K}_D)u^{\star}_{A,+,\mathbf{K}_D}(\mathbf{p})u^{\star}_{B,+,\mathbf{K}_D}(-\mathbf{p})u_{B,+,-\mathbf{K}_D}(-\mathbf{p}'),u_{A,+,-\mathbf{K}_D}(\mathbf{p}'), \tag{141}$$

$$U_4 = U\mathscr{F}(\mathbf{p}-\mathbf{p}')u^{\star}_{A,+,\mathbf{K}_D}(\mathbf{p})u^{\star}_{B,+,\mathbf{K}_D}(-\mathbf{p})u_{B,+,\mathbf{K}_D}(-\mathbf{p}').u_{A,+,\mathbf{K}_D}(\mathbf{p}'). \tag{142}$$

The factor of 2 in the $U_1(\mathbf{p},\mathbf{p}')$ and $U_2(\mathbf{p},\mathbf{p}')$ accounts for the $\mathbf{p}\to\mathbf{p}'$ interaction terms. Each of these terms corresponds to a repulsive interaction that inhibits superconductivity. The interaction matrix elements $U_1(\mathbf{p},\mathbf{p}')$ and $U_2(\mathbf{p},\mathbf{p}')$ correspond to inter-valley scattering and inter-valley exchange interactions, and inhibit inter-valley pairing. The intra-valley interactions $U_4(\mathbf{p},\mathbf{p}')$ and $U_3(\mathbf{p},\mathbf{p}')$ correspond to intra-valley scattering and Cooper pair tunneling processes, which inhibit intra-valley pairing.

For small momentum transfers, $|\mathbf{p}-\mathbf{p}'| \ll 1/a_0$, the lattice form factor $\mathscr{F}(\pm\mathbf{K}_D) = 0$ suppresses the inter-valley exchange and Cooper pair tunneling interactions. Therefore, we simply need to calculate $U_1(\mathbf{p},\mathbf{p}')$ and $U_4(\mathbf{p},\mathbf{p}')$ interaction terms. Since the projected interaction depends on the sublattice index $U_1(\mathbf{p},\mathbf{p}')$ and $U_4(\mathbf{p},\mathbf{p}')$ are not related. The $\alpha = +$ wavefunction for the $\mathbf{K}_D$ and $-\mathbf{K}_D$ valley are,

$$|u_{+,\mathbf{K}_D}(\mathbf{p})\rangle = \begin{pmatrix} u_{\mathbf{p}}e^{-\imath J\varphi_{\mathbf{p}}/2} \\ v_{\mathbf{p}}e^{\imath J\varphi_{\mathbf{p}}/2}\end{pmatrix}, \qquad |u_{+,-\mathbf{K}_D}(-\mathbf{p})\rangle = \begin{pmatrix} v_{\mathbf{p}}e^{\imath J\varphi_{\mathbf{p}}/2} \\ u_{\mathbf{p}}e^{-\imath J\varphi_{\mathbf{p}}/2}\end{pmatrix}, \tag{143}$$

where

$$u_{\mathbf{p}} = \frac{1}{\sqrt{2}}\Big(1+\frac{m}{\sqrt{\zeta_J p^{2J}+m^2}}\Big)^{1/2}, \qquad v_{\mathbf{p}} = \frac{1}{\sqrt{2}}\Big(1-\frac{m}{\sqrt{\zeta_J p^{2J}+m^2}}\Big)^{1/2}, \tag{144}$$

can be used to evaluate the interaction matrix elements. This gives

$$u^{\star}_{A,+,\mathbf{K}_D}(\mathbf{p}) = u_{\mathbf{p}}e^{\imath J\varphi_{\mathbf{p}}/2}, \qquad u^{\star}_{B,+,\mathbf{K}_D}(-\mathbf{p}) = (-1)^J v_{\mathbf{p}}e^{-\imath J\varphi_{\mathbf{p}}/2}, \tag{145}$$

$$u_{A,+,\mathbf{K}_D}(\mathbf{p}') = u_{\mathbf{p}}e^{-\imath J\varphi_{\mathbf{p}'}/2}, \qquad u_{B,+,\mathbf{K}_D}(-\mathbf{p}') = (-1)^J v_{\mathbf{p}'}e^{\imath J\varphi_{\mathbf{p}'}/2}. \tag{146}$$

With this gauge choice, we can calculate the interaction matrix elements near the Fermi surface $p_x = p_F\cos(\varphi_{\mathbf{p}})$, $p_y = p_F\sin(\varphi_{\mathbf{p}})$ and $|\mathbf{p}| \sim |\mathbf{p}'| \sim p_F$, which gives

$$U_1(\mathbf{p},\mathbf{p}') = \frac{3U}{2}\Big(1+\frac{m}{(\xi_p+\mu)}\Big)^2 e^{\imath J(\varphi_{\mathbf{p}}-\varphi_{\mathbf{p}'})}, \qquad U_4(\mathbf{p},\mathbf{p}') = \frac{3U}{4}\Big(1-\frac{m^2}{(\xi_p+\mu)^2}\Big), \tag{147}$$

where we take $\mathscr{F}(0) \simeq 3$. This indicates that the projected repulsive interactions associated with nearest-neighbor interactions only affect the s-wave pairing. In the case of even chirality, the chiral-J Kekulé pairing interaction is unaffected by electron repulsion. However, the s-wave Kekulé is affected, so we expect the phase boundary to shift to higher densities. A similar argument shows that the phase boundary of the odd chiral Kekulé superconductor will also shift to higher densities.

SUPERFLUID STIFFNESS OF THE KEKULÉ SUPERCONDUCTOR

The chiral Kekulé superconducting state corresponds to pairing within each valley with a fully gapped order parameter $\Delta e^{\imath\tau J\varphi_{\mathbf{p}}}$. In the continuum limit, the Kekulé superconducting state can be described by an effective Bogoliubov–de Gennes (BdG) Hamiltonian in each valley, which can be expressed as

$$\mathcal{H}_{BdG}(\mathbf{p},\tau) = \begin{pmatrix} \xi_{\mathbf{p}} & \Delta e^{\imath\tau J\varphi_{\mathbf{p}}} \\ \Delta e^{-\imath\tau J\varphi_{\mathbf{p}}} & -\xi_{-\mathbf{p}} \end{pmatrix}, \tag{148}$$

where $\tau = \pm$ labels the valleys $\mathbf{K}_D$ and $-\mathbf{K}_D$, with Nambu spinors $\psi_{\mathbf{p},+} = (a_{\mathbf{p}}, a^{\dagger}_{-\mathbf{p}})$ and $\psi_{\mathbf{p},-} = (b_{\mathbf{p}}, b^{\dagger}_{-\mathbf{p}})$. This effective BdG Hamiltonian is valid within the bandwidth set by the cutoff momentum $\Lambda \sim 1/a_0$, where the continuum description of chiral 2DEGs provides a good approximation. Due to azimuthal symmetry, the superfluid stiffness tensor satisfies $\rho_{\mu\nu} = \rho\delta_{\mu\nu}$ (with $\mu,\nu = x,y$), and therefore it is sufficient to compute the diagonal component $\rho_{xx} = \rho$. The relation $\rho_{\mu\nu} = \rho\delta_{\mu\nu}$ also holds for systems with C_{3v} symmetry and thus applies to the honeycomb lattice model.

Superfluid stiffness for $m = 0$

Before we move to the case of $m \neq 0$, we begin with the calculation of the superfluid stiffness for the case of a hypothetical Kekulé superconductor with $m = 0$. Assuming that the BdG Hamiltonian is valid up to the cutoff momentum $\Lambda \sim 1/a_0$, and using the formalism developed in Ref. [7], we can calculate the superfluid stiffness for the two-band model. The superfluid stiffness, $\rho = \rho_{conv} + \rho_{geo}$, consists of a conventional contribution (ρ_{conv}) and a geometric contribution (ρ_{geo}). The superfluid stiffness of any two-band model can be written as (see also Ref. [7] for details)

$$\rho = \rho_{conv} + \rho_{geo} = g\sum_{\alpha=\pm}\int \frac{d^2\mathbf{p}}{(2\pi)^2}\frac{\Delta^2}{E^3_{\mathbf{p},J,\alpha}}\partial_x\xi_{\mathbf{p},\alpha}\partial_x\xi_{\mathbf{p},\alpha} + g\sum_{\alpha=\pm}\int \frac{d^2\mathbf{p}}{(2\pi)^2}\frac{2\Delta^2}{\alpha E_{\mathbf{p},J,\alpha}}\frac{\epsilon_{\mathbf{p},J}}{\mu}g_{xx}(\mathbf{p}), \tag{149}$$

where $g = 2$ accounts for the valley degeneracy, g_{xx} denotes the xx-component of the quantum metric, $\alpha = \pm$ labels the bands, and the integral is limited by the cutoff $\Lambda \sim 1/a_0$. For any two-band model, the band-resolved intra- and inter-band quantum metrics satisfy $g^{++}_{\mu\nu}(\mathbf{p}) = g^{--}_{\mu\nu}(\mathbf{p}) = g^{+-}_{\mu\nu}(\mathbf{p})$.

In the absence of a mass term $m = 0$, the quantum metric components can be expressed as

$$g_{\mu\nu}(\mathbf{p}) = \frac{J^2}{2}\left(\frac{p^2\delta_{\mu\nu} - p_\mu p_\nu}{p^4}\right), \tag{150}$$

where $p = \sqrt{p_x^2 + p_y^2}$. The geometric contribution from each band exhibits infrared (IR) divergence, necessitating a regularization scheme. One convenient regularization is to include both bands when calculating the geometric superfluid stiffness. For $m = 0$, the superfluid stiffness can be evaluated analytically. In the weak-coupling limit $\Delta \ll \mu$, it can be written as

$$\rho_0 = \rho(m=0) = \rho_{conv}(m=0) + \rho_{geo}(m=0) = \frac{gJ}{2\pi}\left(\sqrt{\mu_0^2 + \Delta^2}\right) + \frac{gJ\Delta^2}{2\pi\mu_0}\log\left(\frac{\sqrt{\Delta^2 + \mu_0^2} + \mu}{|\Delta|}\right). \tag{151}$$

where $\mu_0 = \mu(m=0) = \zeta_J p_F^J$ denotes the Fermi energy for $m = 0$. This is the same expression as the superfluid stiffness of the inter-valley pairing state in chiral 2DEGs; see Ref. [8] for details. From Eq. 151, it is clear that the geometric contribution to the superfluid stiffness can be neglected in the weak-coupling limit since $\rho_{geo}/\rho_{conv} \propto (\Delta/\mu_0)^2\log(2\mu_0/\Delta)$. Therefore, in the weak-coupling limit, the superfluid stiffness of a chiral 2DEG Kekulé superconductor becomes

$$\rho_0 \simeq \frac{J}{\pi}\mu_0 = \frac{J\zeta_J}{\pi}(2\pi n_e)^{J/2}, \tag{152}$$

where we have used $g = 2$ and expressed $p_F = (2\pi n_e)^{1/2}$, with n_e denoting the electron density. Thus, the superfluid stiffness in a chiral 2DEG scales as $n_e^{J/2}$. It is instructive to compare this result with the superfluid stiffness of a conventional two-dimensional electron gas. Due to Galilean invariance, the superfluid stiffness of a two-dimensional electron gas, $\hbar^2 n_e/m^\star$, is proportional to the electron density. Likewise, in a chiral 2DEG, for $\Delta \ll \mu$, the stiffness is primarily determined by the electron density, with only a weak dependence on the superconducting order parameter Δ.

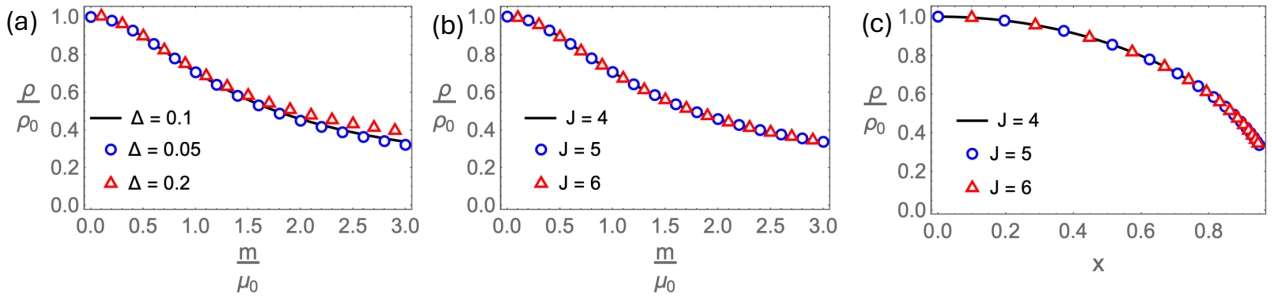


FIG. 7: (a) Superfluid stiffness ratio ρ/ρ_0 calculated as a function of $\tilde{m} = m/\mu_0$, for different values of $\tilde{\Delta} = 0.05, 0.1$ and 0.2 for $J = 4$. (b) Superfluid stiffness ratio ρ/ρ_0 calculated as a function of $\tilde{m} = m/\mu_0$, for different values of $J = 4, 5$ and 6 for $\tilde{\Delta} = 0.1$. (c) Same as (b) but converted to a function of $x = m/\mu$.

Superfluid stiffness for $m \neq 0$

A finite Haldane mass term $m \neq 0$ results in a bandgap $2m$ between the conduction and valence bands. Therefore, in the weak coupling limit $\Delta \ll \mu$, we can focus on the conduction band and calculate the projected superfluid weight, which can be expressed as,

$$\rho = \rho_{conv} + \rho_{geo} = g \int \frac{d^2\mathbf{p}}{(2\pi)^2} \frac{\Delta^2}{E^3_{\mathbf{p},J,+}} \partial_x \xi_{\mathbf{p},+} \partial_x \xi_{\mathbf{p},+} + g \int \frac{d^2\mathbf{p}}{(2\pi)^2} \frac{2\Delta^2}{E_{\mathbf{p},J,+}} g_{xx}(\mathbf{p}). \tag{153}$$

In the weak coupling limit, we find that the conventional contribution to the stiffness is independent of Δ and dominates over the geometric contribution (see discussion below). For $m \neq 0$ and $\Delta/\mu_0 < 0.2$, the superfluid stiffness, which is dominated by the conventional contribution can be expressed as,

$$\rho(m) = \rho_0 h(\tilde{m}) = \frac{J\zeta_J (2\pi n_e)^{J/2}}{\pi} h(\tilde{m}), \tag{154}$$

where h is a scaling function independent of the chirality index J and the order parameter Δ and we define $\tilde{m} = m/\mu_0$. To calculate the scaling function h we express the conventional contribution of the stiffness for the projected conduction band $\alpha = +$ as,

$$\rho(m) = g \int \frac{d^2\mathbf{p}}{(2\pi)^2} \frac{\Delta^2}{\left[\left(\sqrt{\zeta_J^2 p^{2J} + m^2} - \sqrt{\zeta_J^2 p_F^{2J} + m^2}\right)^2 + \Delta^2\right]^{3/2}} \frac{\zeta_J^4 J^2 p^{4J-2}}{(\zeta^2 p^{2J} + m^2)} \sin^2 \varphi_{\mathbf{p}}. \tag{155}$$

Scaling all momenta by p_F and all energy scales by μ_0, we can express the ratio of the superfluid stiffness to the stiffness at $m = 0$ as

$$\frac{\rho(m)}{\rho_0} = h(\tilde{m}) = \left(\frac{\Delta}{\mu_0}\right)^2 \frac{J}{2} \int_0^\infty dy \frac{y^{4J-1}}{[(\sqrt{y^{2J} + \tilde{m}^2} - \sqrt{1 + \tilde{m}^2})^2 + \tilde{\Delta}^2]^{3/2}} \frac{1}{y^{2J} + \tilde{m}^2}, \tag{156}$$

where $\tilde{\Delta} = \Delta/\mu_0$, $\tilde{m} = m/\mu_0$ and $y = p/p_F$. Although the order parameter in the Kekulé superconductor depends on the mass m, in the weak-coupling limit, the superfluid stiffness becomes independent of the interaction strength. Consequently, the stiffness obtained by assuming a constant Δ provides a good approximation to the physical superfluid stiffness.

The scaling function for different values of $\tilde{\Delta} = 0.05, 0.1$, and 0.2 is plotted as a function of $\tilde{m}$ in Fig. 7(a). Figure 7(b) shows the independence of the scaling function on the chirality index J, where we take $\tilde{\Delta} = 0.1$. In Fig. 7(c) we express the result as a function of $x = m/\mu = \tilde{m}/\sqrt{1 + \tilde{m}^2}$. The results show that the stiffness is independent of the value of Δ, and that the same expression for the stiffness applies to both inter-valley and intra-valley superconducting states. In the Kekulé superconducting state, which occurs at $\tilde{m} = 1/\sqrt{3}$, the stiffness is approximately $\rho \approx 0.8\rho_0$. As $\tilde{m}$ increases, the stiffness decreases to $\rho \approx 0.4, \rho_0$ for $\tilde{m} = 3$ ($x \sim 0.95$), but it is still determined by the electron density n_e.

We now show that $\rho_{geo}/\rho_{conv} \propto (\Delta/\mu_0)^2$, so we can neglect the geometric contribution to the stiffness. In the weak-coupling limit, the order parameter is nonzero only within a thin shell near the Fermi surface. Therefore, the integral in the second term of Eq. 153 samples only a small region of phase space. When $-\Delta < \xi_{\mathbf{p},J} < \Delta$, the geometric superfluid stiffness roughly scales with

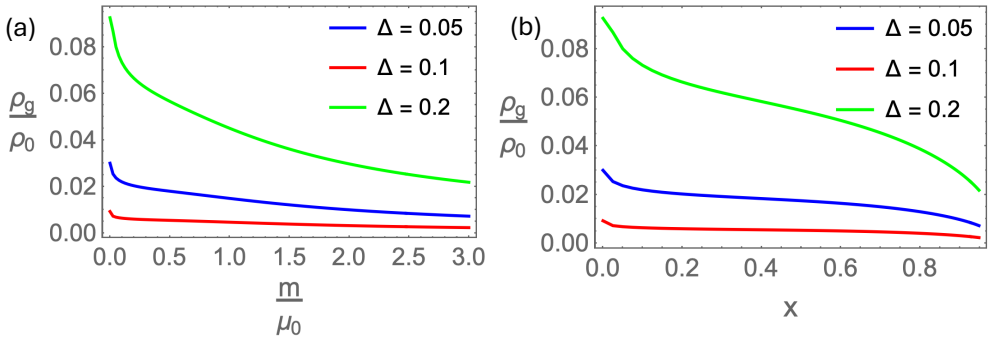


FIG. 8: (a) Geometric Superfluid stiffness ratio ρ_g/ρ_0 calculated as a function of $\tilde{m} = m/\mu_0$, for different values of $\tilde{\Delta} = 0.05, 0.1$ and 0.2 for $J = 4$. (a) Same as (b) but converted to a function of $x = m/\mu$.

Δ. Outside this regime, the contribution vanishes as $\Delta \to 0$. Since the quantum metric is well behaved near the Fermi energy (see Ref. [8] for the expression of the quantum metric in massive chiral 2DEGs), the geometric contribution to the superfluid stiffness is proportional to Δ near the Fermi energy. Based on the arguments above, the calculation of the geometric contribution of the stiffness for a constant Δ over the full bandwidth of the conduction band provides an upper bound on the geometric stiffness for an order parameter which is nonzero within a thin shell near the Fermi surface. The geometric stiffness for a constant Δ is plotted in Fig. 8. Since the geometric stiffness is independent of the chirality J, we just use $J = 4$. Unlike the conventional stiffness, the geometric stiffness scales as $\rho_g/\rho_0 \sim (\Delta/\mu_0)^2$; therefore, its contribution to the stiffness can be ignored. For completeness, we provide the expression of ρ_g/ρ_0 plotted in Fig. 8.

Using the expression of the quantum metric for massive chiral 2DEGs [8],

$$g_{\mu\nu}(\mathbf{p}) = \frac{\zeta_J^2 J^2 p^{2J-2}}{2(\zeta_J^2 p^{2J} + m^2)^2}\left(m^2\delta_{\mu\nu} + \frac{\zeta_J^2(p^2\delta_{\mu\nu} - p_\mu p_\nu)}{p^{2-2J}}\right), \tag{157}$$

we can express the ratio ρ_g/ρ_0 as

$$\frac{\rho_g}{\rho_0} = \left(\frac{\Delta}{\mu_0}\right)^2 \frac{J}{2}\int_0^\infty dy \frac{1}{[(\sqrt{y^{2J}+\tilde{m}^2} - \sqrt{1+\tilde{m}^2})^2 + \tilde{\Delta}^2]^{1/2}} \frac{y^{2J}}{y^{2J}+\tilde{m}^2}\left(\tilde{m}^2 + \frac{y^{2J}}{2}\right). \tag{158}$$

* ybarlas@unr.edu

[1] Y.-Z. Chou, F. Wu, J. D. Sau, and S. Das Sarma, Phys. Rev. Lett. **127**, 187001 (2021).
[2] F. Wu, E. Hwang, and S. Das Sarma, Phys. Rev. B **99**, 165112 (2019).
[3] F. Wu, A. H. MacDonald, and I. Martin, Phys. Rev. Lett. **121**, 257001 (2018).
[4] B. Lian, Z. Wang, and B. A. Bernevig, Phys. Rev. Lett. **122**, 257002 (2019).
[5] C.-X. Liu, Y. Chen, A. Yazdani, and B. A. Bernevig, Phys. Rev. B **110**, 045133 (2024).
[6] T. O. Wehling, E. Şaşıoğlu, C. Friedrich, A. I. Lichtenstein, M. I. Katsnelson, and S. Blügel, Phys. Rev. Lett. **106**, 236805 (2011).
[7] G. Jiang and Y. Barlas, Phys. Rev. B **109**, 214518 (2024).
[8] X. Hu, E. Rossi, and Y. Barlas, Phys. Rev. B **112**, 144502 (2025).